THERMOREFLECTANCE IMAGING AND LIGHT FIELD PROJECTION/PHOTOLITHOGRAPHY

A Dissertation

by

HONGJIE ZHANG

Submitted to the Office of Graduate and Professional Studies of
Texas A&M University
in partial fulfillment of the requirements for the degree of

DOCTOR OF PHILOSOPHY

Chair of Committee,	Sy-Bor Wen
Committee Members,	Philip Hemmer
	Paotai Lin
	David Staack
Head of Department,	Andreas A. Polycarpou

December 2020

Major Subject: Mechanical Engineering

ABSTRACT

Thermoreflectance (TR) imaging is a nonintrusive temperature measurement method which can obtain temperature distribution on target surface with high spatial and temperature resolution. Three-dimensional (3D) TR imaging utilizing light field camera with 4.5 μm lateral resolution and 2.8 μm depth resolution is achieved in this study. With the capability of resolving both light direction and intensity, directional TR signal from tilted or curved surfaces can be measured. Steady–state surface temperature measurements of 3D microscale electronic devices, including 808 nm laser diode and 25 μm gold electric wire, are conducted. The obtained thermal images show that 3D TR imaging can estimate temperature distributions of microscale 3D surfaces that cannot be achieved with traditional two-dimensional (2D) TR imaging.

In the TR imaging experiment, thermal expansion and its associated sample movement, which leads to non-physical temperature values on thermal maps, has been noticed. As a result, a two-wavelength thermoreflectance (2WTR) imaging technique is developed to conduct steady-state temperature measurement of miniature electronic devices. After spatially uniform illumination is achieved (±0.8%), 2WTR imaging obtains temperature information directly from heated target under operation. Therefore, 2WTR is not affected by movement of a heated target due to thermal expansion. Temperature distribution of a microscale gold resistor with 100 nm thickness under steady-state operation are measured via 2WTR (470 and 530 nm), which is challenging to be obtained by single wavelength TR considering the effect of thermal expansion.

A 3D projection system is developed with a microlens array (MLA) and a spatial light modulator (SLM) to perform light field 3D projection. The system collects light beams from multiple SLM pixels onto small voxels of a virtual 3D structure. Algorithm to render SLM pixel value maps is developed using ray tracing method. The projected 3D virtual structure is optically compressed 16X and delivered to an SU-8 photoresist layer for light field 3D photolithography. The fabricated structures have controlled depth change which is not possible in traditional 2D single photon photolithography. Also, the light field 3D photolithography technique has the ability to pattern computer designed microscale 3D structures in a large area ($> 300\ \mu m \times 300\ \mu m$) with fast speed.

DEDICATION

To Mom, Dad and Xin

ACKNOWLEDGEMENTS

First and foremost, I would like to express my sincere gratitude to my committee chair, Dr. Sy-Bor Wen, for his consistent guidance and support throughout the course of this research. I would also like to thank my committee members, Dr. Hemmer, Dr. Lin and Dr. Staack, for their valuable help and suggestions.

Thanks also go to my friends and colleagues, the Mechanical Engineering department faculty and staff, and International Student Services staff for making my time at Texas A&M University a great and rewarding experience.

Last but not least, I would like to thank my parents for their unconditional support and encouragement, and my wife, Xin, for her tremendous patience and love during my years of study.

CONTRIBUTORS AND FUNDING SOURCES

Contributors

This work was supervised by a dissertation committee consisting of Dr. Sy-Bor Wen and Dr. David Staack of the Department of Mechanical Engineering and Dr. Philip Hemmer and Dr. Pao Tai Lin of the Department of Electrical and Computer Engineering.

All work conducted for the dissertation was completed by the student independently.

Funding Sources

This work was made possible in part by National Science Foundation under Grant Number CBET-1545546 and CMMI-1826078. Its contents are solely the responsibility of the authors and do not necessarily represent the official views of the National Science Foundation.

NOMENCLATURE

2D	Two-dimensional
2WTR	Two-wavelength thermoreflectance
3D	Three-dimensional
4D	Four-dimensional
AlGaAs	Aluminum gallium arsenide
CCD	Charge-coupled device
DMD	Digital micromirror device
GaAs	Gallium arsenide
IC	Integrated circuit
IR	Infrared
LCT	Liquid crystal thermography
LED	Light-emitting diode
MEMS	Micro-electro-mechanical system
MLA	Microlens array
SLM	Spatial light modulator
SThM	Scanning thermal microscopy
SU-8	Commonly used permanent epoxy negative photoresist
TDTR	Time domain thermoreflectance
TIR	Total internal reflection
TO	Transistor outline (package)

TR	Thermoreflectance
UV	Ultraviolet
D	Pitch size of microlens array
DR	Digital resolution
DR_L	Digital lateral resolution
DR_z	Digital depth resolution
d	Separation distance from microlens array to spatial light modulator
f	Focal distance of microlens array
h_{conv}	Heat convection coefficient
$\boldsymbol{I}$	Light intensity
i	Microlens distance factor
k	Imaginary part of complex refractive index
k_{glass}	Thermal conductivity of glass
k_{gold}	Thermal conductivity of gold
M	Magnification ratio
NA	Numerical aperture
$\boldsymbol{n}$	Surface normal vector
n	Real part of complex refractive index
$\bar{n}$	Complex refractive index
OR	Optical resolution
OR_L	Optical lateral resolution
OR_z	Optical depth resolution

p	Camera pixel size
R	Reflected light intensity after heating
R_0	Reflected light intensity before heating
s	Pixel size of spatial light modulator
T_0	Temperature before heating
α	Parameter limiting the use of outer portion of each microlens
β	Parameter limiting the use of center portion of each microlens
ΔT	Temperature difference after and before heating
Δx	Lateral voxel size induced by spatial light modulator pixels
Δz	Voxel size in depth induced by spatial light modulator pixels
δx	Lateral voxel size induced by convergence/divergence of light
δz	Voxel size in depth induced by convergence/divergence of light
θ	Angle of incidence
θ_{proj}	Largest angle of light rays converging to a voxel in microscale
θ_R	Largest angle of light rays converging to a voxel in macroscale
κ	Thermoreflectance coefficient
λ	Wavelength
ρ	Reflectivity

TABLE OF CONTENTS

Page

LIST OF FIGURES

Page

LIST OF TABLES

Page

1. INTRODUCTION

1.1. Thermoreflectance Imaging

Following the development of modern electronics industry, the sizes of electronic and optoelectronic components are reduced to as small as a few micrometers. In addition, miniature electronic and optoelectronic components can be assembled in a high packaging density integrated circuit with high power generation. Excess heat generation during operation of microscale electronic devices has become a major concern since the heat generation can induce thermal stress and cause failures [1,2]. More than 50% of the failure in electronic components occurs due to lack of cooling and unexpected temperature [3]. As a result, thermal management [4,5] of such devices becomes critical and challenging. An accurate and convenient measurement of the temperature distribution of the target system is required and can play an important role in the design of optimal thermal management of micro-electronic and micro-optical devices.

1.1.1. Existing Microscale Thermometry and Thermography

Existing microscale thermometry and thermography techniques [6-8], which have been practically used, include but are not limited to micro-thermocouples, infrared (IR) thermometry [9,10], liquid crystal thermography (LCT) technique [11,12], scanning thermal microscopy (SThM) [13,14], Raman spectroscopy [15,16] and thermoreflectance (TR) imaging [17,18].

Micro-thermocouple measurement is a popular method based on Seebeck effect which requires direct contact. Micro-thermocouples can measure temperatures in a wide range from 3 K to 2000 K [19]. Temperature resolution of micro-thermocouples can reach $\sim 0.01\ K$ which is determined by the thermoelectric sensitivity of the metals used in thermocouples. The spatial resolution is limited by the size of wires, which are in tens of micrometers for commercially available micro-thermocouples. When thin film micro-thermocouples are used, the spatial resolution of micro-thermocouples can be better than $400\ nm$ [20]. During the temperature measurement with micro-thermocouples, thermal mass of the thermocouples may possibly affect target temperature especially for microscale targets because of the direct contact [21]. Also, as a point measurement, it requires a large area point-by-point scanning [22] to achieve thermal imaging purpose which is a time-consuming process.

IR thermography is another common method which provides temperature distribution of the target via recording IR emission from surfaces. IR thermography provides real-time thermal map to locate hot spots of heated targets. Spatial resolution of IR thermography, which is determined by the diffraction limit, can hardly reach sub-micron level due to the diffraction limit. For most mid-wave or long-wave IR cameras, wavelength used are longer than 3 μm. One exception would be near IR night vision cameras which use a wavelength from $700\ nm$ to $1000\ nm$, and have spatial resolution in sub-micrometer range. Temperature resolution of IR thermography ranges from $0.02\ K$ to $1\ K$ [23] depending on type of IR detector and the surface condition of target. Also, IR

thermography can have additional errors due to attenuation of the radiation and uncertainty of target emissivity [24].

TR imaging is a non-contact imaging method based on the temperature dependence of reflectivity on material surfaces. A light source is required in TR imaging. Measurement of the change in the reflectivity of the sample needs to be done first in order to obtain the change (increase or decrease) in the temperature of the target. The change in reflectivity can be related to the change in temperature via TR coefficient [25]. One challenging part of TR imaging is that the dependence is weak and thus TR coefficients are usually small. TR coefficients are on the order of $10^{-6}\sim10^{-3}K^{-1}$ [26] from ultraviolet to infrared range for most common metals and semiconductors of interest. As an optical method, the spatial resolution of TR is determined by the diffraction limit. Since visible light is used, the spatial resolution can reach sub-micrometer range. Temperature resolution of TR imaging is determined by TR coefficient and sensitivity of camera sensors, which can be better than $0.01\ K$.

Table 1.1 is a comparison of the three temperature measurement methods mentioned above. Depending on the requirement of applications, a feasible method should be chosen. In this study, TR is selected to thermally study microscale targets with a dimension of a few micrometers because TR is not only a non-intrusive method which does not affect the heat transfer on the target, but also an imaging method which can obtain the temperature distribution on target surface with high spatial, temporal and temperature resolution.

Table 1.1 Comparison of three common microscale temperature measurement methods

	Contact/Non-contact	Imaging method	Spatial resolution	Temperature resolution
Micro-thermocouples	Contact	No	≤0.4 μm	0.01 K
Infrared (IR) thermography	Non-contact	Yes	0.7-10 μm	0.02-1 K
Thermoreflectance (TR) imaging	Non-contact	Yes	0.3-0.5 μm	0.01 K

1.1.2. Development of Thermoreflectance Imaging

TR imaging achieves non-intrusive temperature measurement by detecting the change of reflectivity of target surfaces when there are temperature variations. In traditional TR imaging, a single wavelength probe beam is required to illuminate the target and to induce the reflection signal. An optical detector is responsible for determining the reflection signal change from the target surface before and after heating. The change of the reflection signal can be linked to the change of the surface temperature with TR theory, based on the fact that changes in refractive index and reflectivity of the material are almost linear functions of the surface temperature change [27,28]. For metals, a small increase in temperature alters the optical properties of in various ways [29]: Volume thermal expansion causes shifts and warping in electron energy bands; The phonon population increases, which decreases electron relaxation times through electron-phonon interaction; The step in the Fermi distribution broadens, which affects interband transitions.

TR in semiconductors [30-33] and conductors [34] were first studied and was later introduced for point temperature measurement [35,36]. TR then grew into a thermography technique when photodiode array [37] and charge-coupled device (CCD) [38] was adopted as detectors. Two-dimensional (2D) TR thermography has the ability of reaching $< 0.1\ K$ temperature resolution and $300\ nm$ spatial resolution [39,40]. TR measurement can be done within a wide but finite temperature range [41], usually several hundred Kelvin above or below the reference temperature. Time domain thermoreflectance (TDTR) [42-44] was also developed recently to determine transient temperature distribution for 2D target surfaces with nanosecond level or higher time resolution [45].

1.2. Microlens Array Based Light Field Imaging

The intensity of light traveling along a ray is denoted by I and measured in watts (W) per steradian (sr) per square meter (m^2). For monochromatic and steady-state light, I is a four-dimensional (4D) function as $I = I(x, y, \theta, \varphi)$ where (x, y) is the spatial location and (θ, φ) is the direction of light ray. The 4D light intensity is also called photic field or 4D light field. To reconstruct the surface of a 3D target object for imaging, light field information should be obtained by recording the intensity and direction of the light field at any imaging plane. Light field cameras were developed to achieve 3D imaging.

Microlens array (MLA) based light field cameras, or plenoptic cameras, are popular in 3D imaging and are adopted in this study to capture 3D surface images. Two versions of MLA based light field camera, namely, unfocused light field camera (plenoptic camera 1.0) and focused light field camera (plenoptic camera 2.0), have been developed.

Unfocused light field camera [46,47], or plenoptic camera 1.0, inserts a microlens array at the image plane of the main camera lens of a conventional 2D camera. The image sensors are located one focal length behind the microlenses. The light field imaging technique was extended by introducing more efficient analysis for fast light field processing and refocusing [48]. In unfocused light field camera, the sensors beneath a microlens provide directional information at that point. However, each microlens captures only the light from a single spatial point, which limits the spatial resolution of unfocused light field camera.

To solve this issue, focused light field camera, or plenoptic camera 2.0, was developed [49]. Instead of focusing the main lens at the MLA, focused light field camera places MLA before/after the focusing plane of the main lens and produces a set of relay systems. Depending on the location of the main image relative to the MLA, there are two different modes [50] of MLA based focused light field cameras: Keplerian mode or Galilean mode as shown in Figure 1.1. The configuration of a focused light field camera is shown in Figure 1.2, which is the optical path of one Galilean mode focused light field camera, i.e. main image of the object is behind MLA. This improved configuration, compared with the unfocused light filed camera, produces a flexible trade-off in the spatial and angular resolution, and allows positional information in the radiance to be sampled more effectively. Moreover, a focused light field camera with extended depth of field was developed [51] by introducing MLA with multiple types of microlenses, and also commercially available.

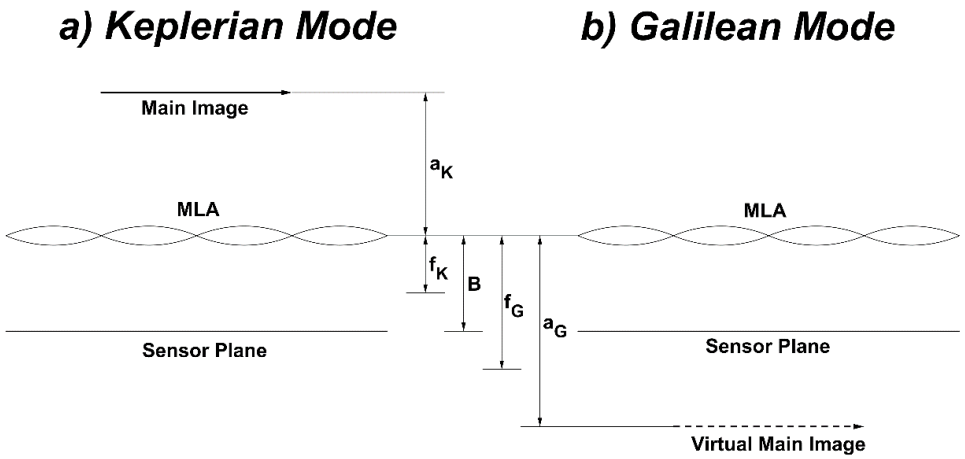

Figure 1.1 Two different modes of focused light field camera: a). Keplerian mode; b). Galilean mode. Here, *a* indicates the location of main image formed by the main lens; *B* is the separation distance from microlens array (MLA) to sensor plane; f is the focal distance of each microlens; subscripts *K* and *G* are for Keplerian mode and Galilean mode, respectively.

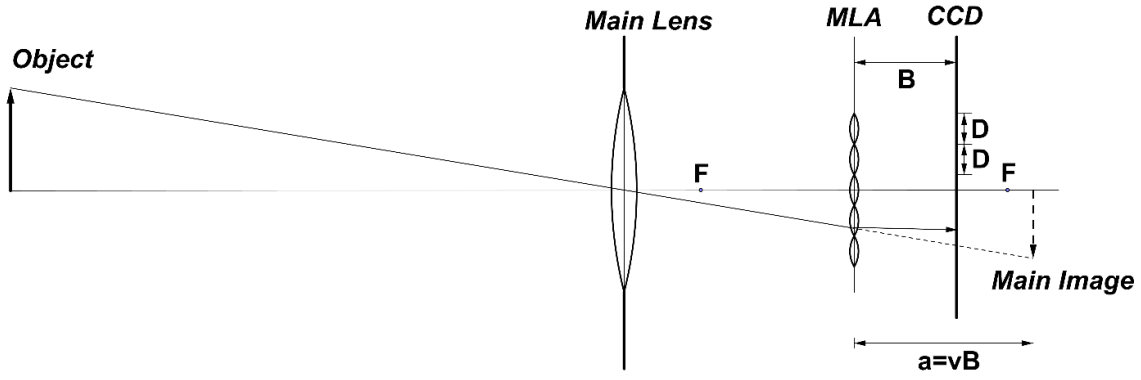

Figure 1.2 Schematic of the Galilean mode focused light field camera, where *a* indicates the location of main image formed by the main lens; *B* is the separation distance from MLA to charge-coupled device (CCD) sensor plane; *D* is the size of each microlens; *F* is the focal point of microlens.

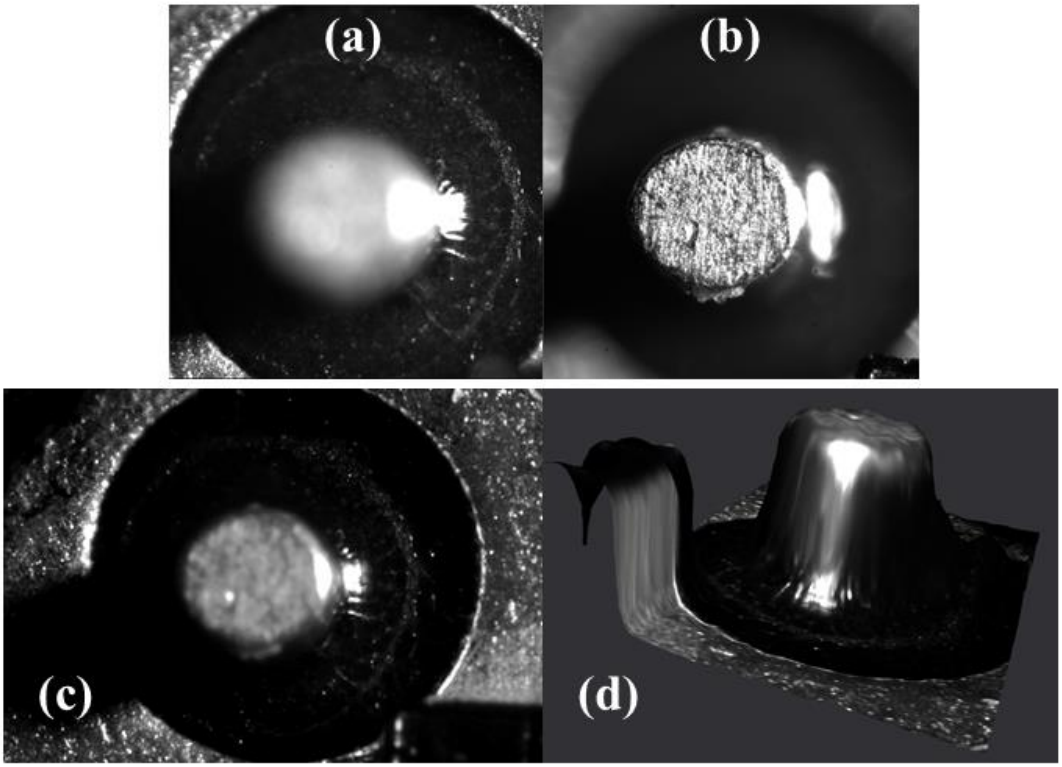

Figure 1.3 Images of a transistor outline package, case style 18 (TO-18) transistor case taken by conventional two-dimensional (2D) camera (Opteon 1000 base T camera) focused on (a). base plane; (b). top surface; and by MLA based light field camera (R10μ, Raytrix GmbH) with (c). total focused image and (d). reconstructed three-dimensional (3D) depth map.

The advantage of light field imaging is that it can provide an extended depth of field compared with conventional 2D imaging. Figure 1.3 presents the images of the same target, a transistor outline package, case style 18 (TO-18) transistor case, taken by conventional 2D camera (Opteon 1000 base T camera) and light field camera (R10μ, Raytrix GmbH), respectively. Figure 1.3(a) focus on the base of TO-18 transistor case while the top surface is blurred. Figure 1.3(b) shows the opposite, which indicates the traditional 2D camera can only focus in a very small depth range. On the other hand, the

3D reconstructed images from light field camera, Figure 1.3(c) and (d), obviously have an extended depth of view, when the 3D depth map can be reconstructed and refocused at different depths.

1.3. Three-Dimensional Photolithography

Following the demand of integrated circuit (IC), microelectronics, micro-electro-mechanical systems (MEMS), and micro-bio devices, various microfabrication techniques have been proposed and demonstrated [52-57]. Such techniques include electron beam lithography [58-60], focused ion beam [61-63], photolithography [64,65], etc. In addition to 2D patterning, 3D lithography also attracts significant attention due to the potential miniaturization of microelectronics and MEMS devices with 3D structures [66]. Compared with their 2D counterparts, 3D microstructures can significantly reduce weight-to-performance ratio for same task [67]. Also, 3D microstructures can have unique mechanical, electrical and optical properties that do not exist in 2D microstructures [68,69].

Different 3D lithography methods have been developed. For example, stereolithography can achieve 3D patterning through layer-by-layer additive manufacturing [70-75]. The spatial resolution of layer-by-layer stereolithography is limited by laser beam spot size and minimum incremental distance of the controllable stage. As an additive process with layer-by-layer sequence, stereolithography requires a large number of perpendicular movements to fabricate a 3D structure. Supporting frames are commonly required in stereolithography to pattern free standing structures [76].

Holographic lithography [77-81] is a 3D patterning method without need of scanning or layer stacking, which can pattern 3D structures in single projection. In holographic lithography, a hologram is constructed or computer generated to record the interferences of the diffracted beam from an object and a coherent reference beam [82]. A collimated illumination beam, which is in phase conjugate to the reference beam, is then diffracted from the hologram to reproduce the original image. Holographic lithography can fabricate 3D structures with higher speed compared with stereolithography. However, the required coherent light can easily create speckles [83] which can significantly reduce the spatial resolution and quality in 3D holographic fabrications. The speckles are formed because imperfect surfaces of optical components induce distortion of wave front and reflection, which interfere with the incoming laser beam.

Another common method in 3D fabrication is through single spot multi-photon photolithography [84-88] via scanning of a femtosecond laser spot in designed 3D regions. With multi-photon absorption [89,90], sub-diffraction-limit spatial resolution down to $100\,nm$ (or better) can be successfully achieved with single spot multi-photon photolithography [91]. However, using single spots to pattern a large 3D region requires high speed translation stages or Galvo scanning mirror pairs [92], which could be time consuming. Efforts have been made to improve the fabrication throughput in multi-photon photolithography. For example, multiple-spot parallel processing has been introduced in multi-photon photolithography [93]. However, such approach is limited to periodic patterns.

Table 1.2 Comparison of three common 3D lithography techniques

	Spatial resolution	Scanning required
Single spot multi-photon photolithography	≤ 100 nm	Yes, point-by-point
Stereolithography	< 1 μm	Yes, layer-by-layer
Holographic lithography	>1μm for complicated structures	No

1.4. Scope of the Dissertation

This dissertation begins with a literature review of TR imaging including comparison of microscale temperature measurement methods and current development of TR imaging research. TR imaging is one main topic of this dissertation and is studies in Chapter 2 and 3. It is followed by an introduction of microlens array based light field imaging/camera, which is the optical device used in Chapter 2 for developing 3D TR imaging. A review and comparison of existing three-dimensional photolithography techniques is also listed, as light field 3D projection and photolithography in Chapter 4 is the other main topic of this dissertation.

In Chapter 2, a new 3D TR imaging method that can conduct steady-state surface temperature measurement of microscale electronic devices with 3D tilted or curved surfaces are presented. This objective is achieved by using light field camera as the optical detector (Section 2.2) and characterizing the directional dependence of material surface TR coefficient (Section 2.3). Experimental setup is described in Section 2.4 and results are discussed in Section 2.5.

In Chapter 3, a new two-wavelength TR (2WTR) method/system that can overcome the thermal expansion related movement issue in the traditional single wavelength TR technique is proposed and examined. Theory of 2WTR is presented in Section 3.2. With the programmable spatial light modulator (SLM) light source, an iterative scheme is designed to provide uniform illumination for the sample in Section 3.3. 2WTR temperature measurement results are discussed in Section 3.4. The 2WTR thermal maps shows the temperature measurement is not affected by thermal expansion, which is an issue traditional single wavelength TR suffers from.

In Chapter 4, an optical design/system which can perform light field 3D projection and single photon 3D photolithography with the implementation of a MLA and a SLM is established. Section 4.2 presents the optical design and mathematical algorithm to render pixel value map in detail. The experimental setup and MLA-SLM calibration procedures are described in Section 4.3. Lateral and depth resolution of the 3D system is estimated in Section 4.4. The light field 3D projection and photolithography results are discussed in Section 4.5. The 3D photolithography technique is proved to have the capability of 3D microfabrication with large area and fast speed.

Chapter 5 is a conclusion on the contributions of this dissertation and possible future study related to this dissertation.

2. THREE-DIMENSIONAL THERMOREFLECTANCE IMAGING*

2.1. Motivation

Existing TR imaging uses conventional 2D camera as optical detector which has limited depth of field. The limited depth of field causes difficulty for measuring 3D targets with curved/tilted surface. Also, in traditional TR theory, normal incidence of light is required, therefore TR coefficient is not a function of incident light angle. Normal incidence is true for large 2D plane surfaces, however is not true in 3D microscale cases. As the miniaturization and compact packaging of microscale electronic devices, most components appear as 3D structures. With the strong needs to accurately measure temperature profiles on the surfaces of 3D microscale electronic devices, 3D TR imaging would be valuable for the thermal management of such devices. Hence, this chapter is to introduce a new 3D TR technique through combining existing TR thermography with 3D imaging techniques, i.e. microlens array based light field imaging. As illustrated in Section 1.2, light field cameras can not only reconstruct curved and tilted 3D surfaces, but also provide an extended depth of field, which is useful in developing a 3D TR imaging technique.

---

*Part of this chapter is reprinted with permission from "Temperature measurement of microscale electronic devices with 3D thermoreflectance imaging." by Zhang, Hongjie and Sy-Bor Wen. ASME. Heat Transfer Summer Conference, Volume 1, 2017. Copyright 2017 by ASME.

2.2. Performance of Multi-focus Light Field Camera

Multi-focus light field camera is a type of focused light field camera which has a MLA consisting of microlens with three different focal lengths. The three types of microlenses are arranged in a hexagonal array, as shown in Figure 2.1, which also illustrate the schematic of a multi-focus light field camera working with infinity-corrected microscope setup. Virtual depth of any point on the object is defined as

$$v = \frac{a}{B} \tag{2.1}$$

where a is indicates the location of main image with respect to MLA and B is the separation distance from MLA to CCD sensor plane. The original location of the point on the object is denoted by total distance T, which is the distance from the point to the reference plane. The reference plane is located B away behind the CCD sensor plane. a_{10} indicated the conjugate of the reference plane in object space. T is a bijective function of virtual depth v and the correlation can be determined by ray optics. Thus, we are able to trace every point on the main image back to the object space. Here, D is the size of each microlens. F is the focal point of microlens. The microscope consists of objective lens with focal distance f_1 and tube lens with focal distance f_2. a_1 is the object distance from objective lens; b_2 is the distance from the virtual main image to tube lens. The separation distance from the objective lens and the tube lens is d. The three different type of microlenses L_i has focal distances f^i, $i = 1,2,3$. For the objective lens and tube lens, thin lens equations are satisfied:

$$\frac{1}{a_1}+\frac{1}{b_1}=\frac{1}{f_1} \tag{2.2}$$

$$\frac{1}{a_2}+\frac{1}{b_2}=\frac{1}{f_2} \tag{2.3}$$

The following parameters are given in Figure 2.1 to calculate the performance of light field camera: $f_1 = 40\ mm, f_2 = 200\ mm, d = 100\ mm, a_{10} = 40\ mm, d = 0.126\ mm,$ $B = 3.55\ mm, f^1 = 5.81mm, f^2 = 4.88mm, f^3 = 5.15mm.$

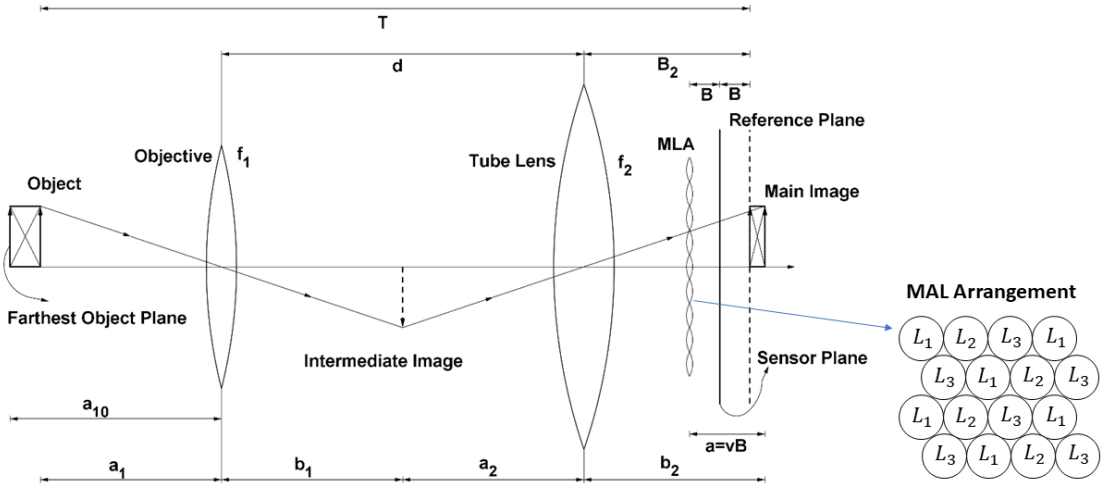

Figure 2.1 Imaging process of the multi-focus light field camera working with a microscope.

Field of view in the multi-focus light field camera is a function of object location. The extent of the observable region on the reference plane is fixed for light field camera and we denote it by $W_2 \times H_2$. The subscript 2 is used since virtual depth of the reference plane is 2. The field of view $W \times H$ on any object plane can thus be calculated by shrinking the extent $W_2 \times H_2$ back to the object space.

$$W = \frac{a_1}{b_1}\frac{a_2}{B_2}W_2 \tag{2.4}$$

$$H = \frac{a_1}{b_1}\frac{a_2}{B_2}H_2 \tag{2.5}$$

The light field camera has pixel size $p = 2.24\ \mu m$ and a total of $N_w \times N_h = 3840 \times 2672$ pixels on the sensor plane, therefore the camera has a theoretical total of approximately 10 million pixels. However, the effective resolution of the light field camera falls below this amount due to three main reasons:

(i) Diffraction limit derived from point spread functions $q = 1.22\lambda N$, where λ is the wavelength and N is the working f number. If the diffraction limit q is larger than the pixel size p, the minimum resolvable size will be bigger than expected.

(ii) Each microlens images a small portion of the entire field of view. For each microlens, the actual location of the micro image may be different from the location of sensor plane. This difference will also increase the minimum resolvable size to $\left|D\left(B/f^i + 1/v - 1\right)\right|$.

(iii) To get depth information, any point on the target must be imaged by at least two microlenses. Multiple pixels on the sensor plane will be imaging an identical point on the object, which will cause the reduction of resolution. The region that can be "seen" by one microlens is expanding as a projection cone in space. Hence, points on a plane that have a virtual depth v are not "seen" by a same number of microlenses. The average number of microlenses that can image one point on the virtual depth v plane is $\xi(v)$.

Combine the effect of all the three points, and we obtain the final expression for effective resolvable divisions M_w in width and M_h in height,

$$M_w = \frac{p}{max\left\{p, q, \left|D\left(\frac{B}{f^i} + \frac{1}{v} - 1\right)\right|\right\}} \frac{1}{\xi(v)} N_w \tag{2.6}$$

$$M_h = \frac{p}{max\left\{p, q, \left|D\left(\frac{B}{f^i} + \frac{1}{v} - 1\right)\right|\right\}} \frac{1}{\xi(v)} N_h \tag{2.7}$$

Based on Equation (2.4) to (2.7), we can further derive the minimum resolvable lateral size ε and effective pixel count M

$$\varepsilon = \frac{W}{M_w} = \frac{H}{M_h} \tag{2.8}$$

$$M = \frac{WH}{\varepsilon^2} \tag{2.9}$$

As shown in Figure 2.2, each type of microlenses for a specific focal length gives a U-shaped curve for lateral resolution, but each U-shaped curve works best in a different depth range. Multi-focus light field camera with 3 types of microlenses would enlarge the high-resolution region and therefore extend depth of field.

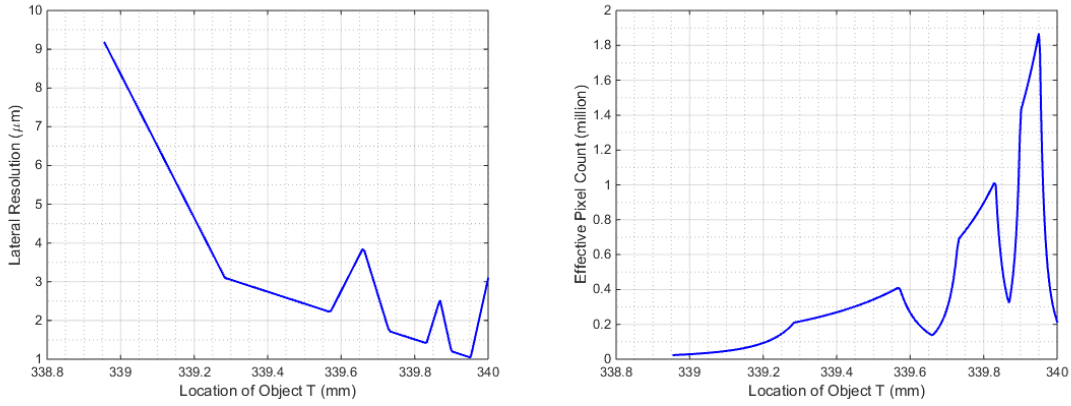

Figure 2.2 Lateral resolution and effective pixel count of a multi-focus light field camera

2.3. Directional Dependence of Thermoreflectance Coefficient

In TR theory, when a sample surface is illuminated with light at wavelength λ, the reflected light intensity can be changed from R_0 to R when the surface temperature is changed from T_0 to $T_0 + \Delta T$. The relative change of the reflected light intensity can be approximated as a linear correlation of temperature change:

$$(R - R_0)/R_0 = \kappa \Delta T \tag{2.10}$$

Here κ is the TR coefficient for a specific material illuminated at wavelength λ. TR coefficients are on the order of $10^{-6}\sim10^{-3}K^{-1}$ from ultraviolet to infrared range for most common metals and semiconductors of interest.

In order to obtain the expression for 3D TR equations, reflection of light at the interface between two materials is considered. Metals are absorbing medium having a non-zero extinction coefficient, or the imaginary part of complex refractive index $\bar{n} = n - ik$. Complex refractive index $\bar{n}$ is a function of propagating light wavelength as well as a weak function of the material temperature. By assuming the incident light has a wavelength λ and incident angle θ with vacuum as background, the reflectivity ρ at the interface can be derived [94]. Here, the subscripts $\perp$ and $\parallel$ indicate s and p polarization, respectively. If the incident light has no specific polarization, the reflectivity is the average of the perpendicular and parallel components.

$$\rho_{\perp,\lambda,\theta}(n,k) = \frac{a^2 + b^2 - 2a\cos\theta + \cos^2\theta}{a^2 + b^2 + 2a\cos\theta + \cos^2\theta} \tag{2.11}$$

$$\rho_{\parallel,\lambda,\theta}(n,k) = B\rho_{\perp,\lambda,\theta}(n,k) \tag{2.12}$$

where

$$a^2 = \frac{1}{2}\left\{[(n^2 - k^2 - \sin^2\theta)^2 + 4n^2k^2]^{\frac{1}{2}} + (n^2 - k^2 - \sin^2\theta)\right\} \tag{2.13}$$

$$b^2 = \frac{1}{2}\left\{[(n^2 - k^2 - \sin^2\theta)^2 + 4n^2k^2]^{\frac{1}{2}} - (n^2 - k^2 - \sin^2\theta)\right\} \tag{2.14}$$

$$B = \frac{a^2 + b^2 - 2a\sin\theta\tan\theta + \sin^2\theta\tan^2\theta}{a^2 + b^2 + 2a\sin\theta\tan\theta + \sin^2\theta\tan^2\theta} \tag{2.15}$$

If there is a slightly change in temperature, the two components of refractive index will change by Δn and Δk accordingly. As a result, the change of reflectivity $\Delta\rho$ is

$$\Delta\rho_{\lambda,\theta}(n,k) = f_{\lambda,\theta}(n,k)\Delta n + g_{\lambda,\theta}(n,k)\Delta k \tag{2.16}$$

where

$$f_{\lambda,\theta}(n,k) = \frac{\partial\rho_{\lambda,\theta}(n,k)}{\partial n} \tag{2.17}$$

$$g_{\lambda,\theta}(n,k) = \frac{\partial\rho_{\lambda,\theta}(n,k)}{\partial k} \tag{2.18}$$

Note that we neglect the subscripts $\perp$ and $\parallel$ in Equation (2.16) for simplicity and the incidence can be either s or p polarized.

The relative change of reflectivity

$$\frac{\Delta\rho_{\lambda,\theta}(n,k)}{\rho_{\lambda,\theta}(n,k)} = \left[\frac{f_{\lambda,\theta}(n,k)}{\rho_{\lambda,\theta}(n,k)}\frac{dn}{dT} + \frac{g_{\lambda,\theta}(n,k)}{\rho_{\lambda,\theta}(n,k)}\frac{dk}{dT}\right]\Delta T \tag{2.19}$$

The directional TR coefficient is defined as

$$\kappa_{\lambda,\theta} \triangleq \frac{f_{\lambda,\theta}(n,k)}{\rho_{\lambda,\theta}(n,k)}\frac{dn}{dT} + \frac{g_{\lambda,\theta}(n,k)}{\rho_{\lambda,\theta}(n,k)} \tag{2.20}$$

The thermo-optic coefficients dn/dT and dk/dT for common materials can be obtained from experiments [95] by spectroscopic ellipsometry. Equation (2.20) defines the expression for TR coefficient of a particular wavelength and incident angle. $\kappa_{\lambda,\theta}$ is a

strong function of wavelength and direction of incident light, but a weak function of temperature. The final expression of $f_{\lambda,\theta}(n,k)$ and $g_{\lambda,\theta}(n,k)$ for s and p polarizations are given as follows,

$$f_{\perp,\lambda,\theta}(n,k) = \frac{4\cos\theta\left\{a\left[\frac{\partial(a^2)}{\partial n}+\frac{\partial(b^2)}{\partial n}\right]-(a^2+b^2+\cos^2\theta)\frac{\partial a}{\partial n}\right\}}{(a^2+b^2+2a\cos\theta+\cos^2\theta)^2} \tag{2.21}$$

$$g_{\perp,\lambda,\theta}(n,k) = \frac{4\cos\theta\left\{a\left[\frac{\partial(a^2)}{\partial k}+\frac{\partial(b^2)}{\partial k}\right]-(a^2+b^2+\cos^2\theta)\frac{\partial a}{\partial k}\right\}}{(a^2+b^2+2a\cos\theta+\cos^2\theta)^2} \tag{2.22}$$

$$f_{\parallel,\lambda,\theta}(n,k) = \rho_{\perp,\lambda,\theta}\frac{\partial B}{\partial n} + Bf_{\perp,\lambda,\theta} \tag{2.23}$$

$$g_{\parallel,\lambda,\theta}(n,k) = \rho_{\perp,\lambda,\theta}\frac{\partial B}{\partial k} + Bg_{\perp,\lambda,\theta} \tag{2.24}$$

where a, b and B can be found in Equation (2.13) to (2.15). Figure 2.3 shows the calculated TR coefficient of gold at 532 nm green illumination with different incident angles for both p and s polarization.

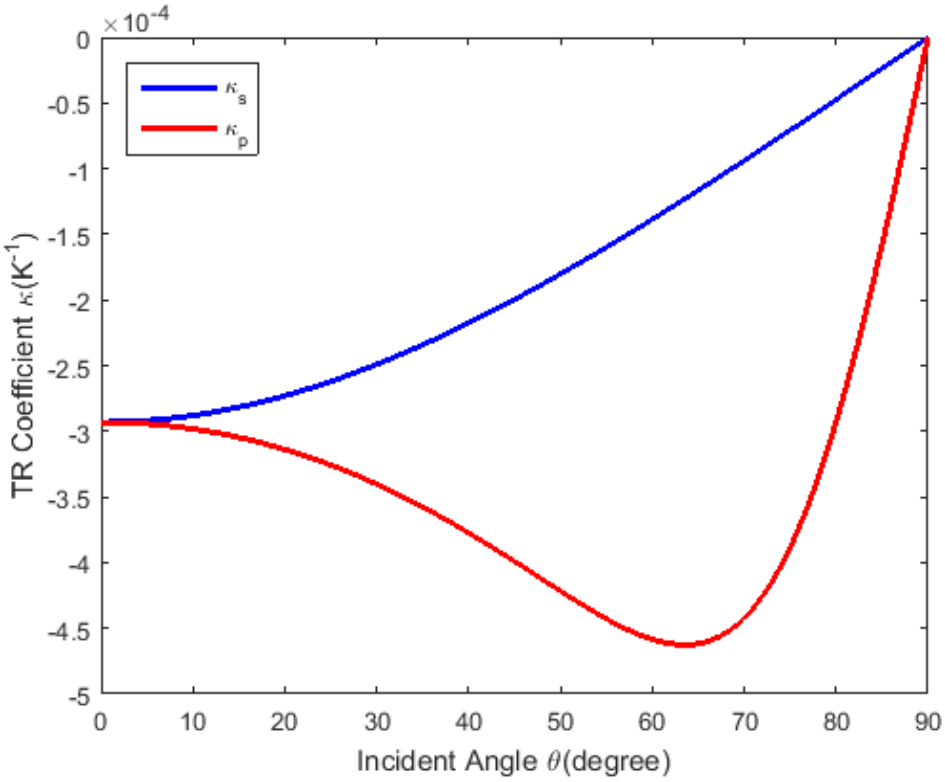

Figure 2.3 Directional dependence of thermoreflectance coefficient for gold illuminated at $532\ nm$.

2.4. Experimental Setup and Procedures

An infinity-corrected microscope system with a 200mm tube lens shown in Figure 2.4 is used in 3D TR imaging of microscale targets. The view lens is either a Nikon AF Nikkor camera view lens (approximately 5X) or a 10X long working distance objective depending on which magnification ratio is required. A R10µ light field camera (Raytrix GmbH) is used as the light field recorder. MLA inside the R10µ camera was calibrated for the current system setup. Figure 2.5 gives two sample images with 3D reconstruction of a MEMS micro-hotplate and its electrode.

After light field is recorded by the plenoptic camera, a depth map could be generated by extracting the depth information. Therefore (x, y, z) location of any point on the target surface in the object space can be obtained. The surface normal $\boldsymbol{n}(x, y, z)$ at that point can then be calculated. Assuming the incident light $\boldsymbol{I}$ toward the surface is along the optical axis, we may therefore get the incident angle at that location

$$\theta(x, y, z) = \langle \boldsymbol{n}, I \rangle = \cos^{-1}\left(\frac{\boldsymbol{n} \cdot I}{|\boldsymbol{n}||\boldsymbol{I}|}\right) \tag{2.25}$$

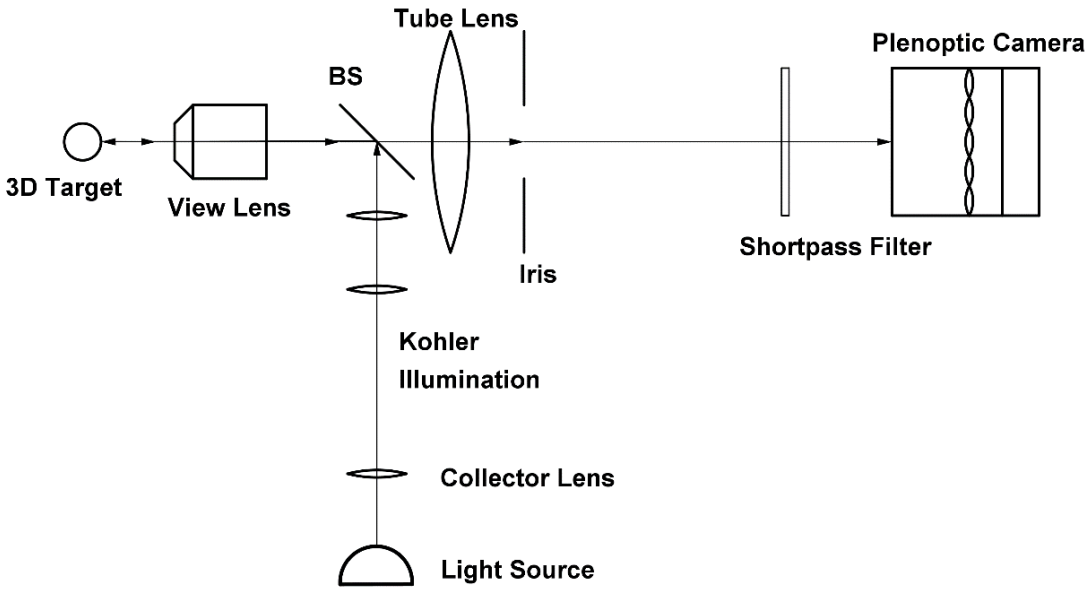

Figure 2.4 Schematic of the experimental setup for three-dimensional (3D) thermoreflectance (TR) imaging.

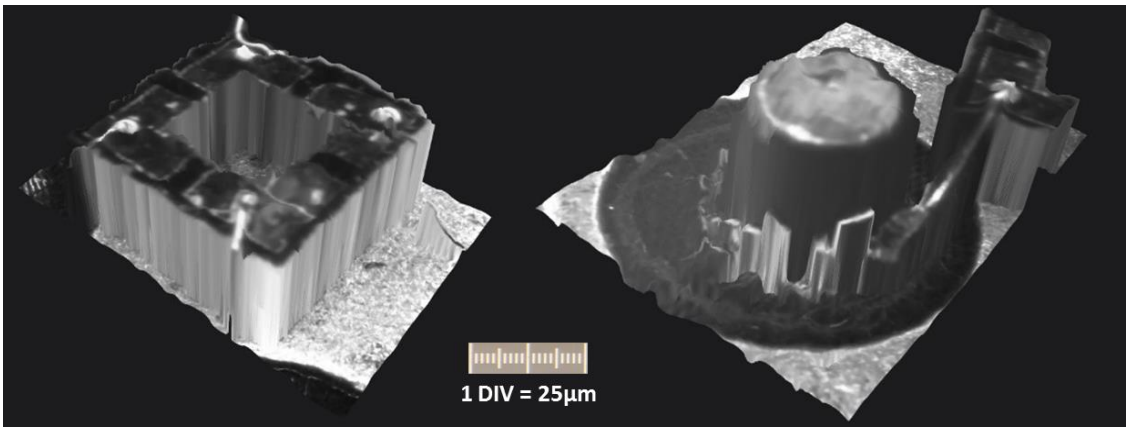

Figure 2.5 Surface reconstruction of the micro-hotplate and electrode.

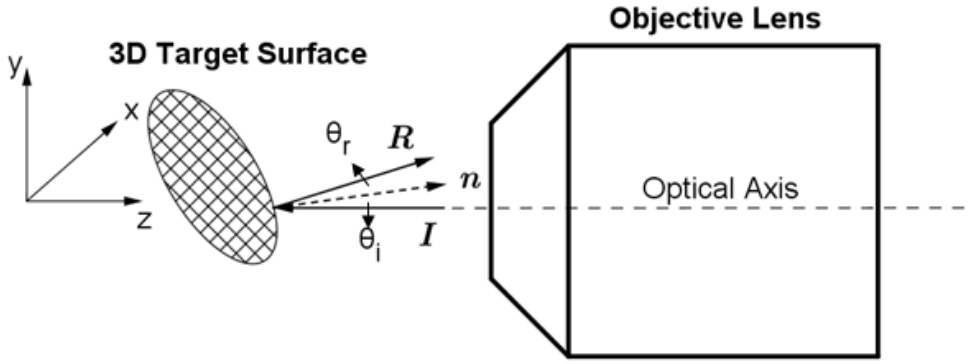

Figure 2.6 Illustration of coordinate system, surface normal vectors and incident angles.

Furthermore, the local TR coefficient can be calculated from the incident angle as shown in Figure 2.6. To get the intensity of reflection, the total focused images are considered. A total focused image is an image that is focused on the calculated depth map. Since thermal radiation and other undesired light rays are filtered out by the shortpass filters placed before the camera, the pixel values in the total focused image collected and generated by the plenoptic camera contain only the intensity of reflection on the target

surface. To better cancel out noise, a series of 5000 heated images as well as a series of 5000 unheated images are taken and averaged. Relative change of the reflectivity can therefore be carried out. Based on Equation (2.19), temperature change between heated and unheated conditions can be estimated after obtaining both the direction TR coefficient and relative change of reflectivity of the 3D surface.

Based on the TR equation (2.10), the temperature resolution is $\Delta T = (2^{12}|\kappa|)^{-1}$ with 12-bit depth CCD camera for data collection and 12-bit data processing as well. For gold at $532\,nm$, $\kappa = -2.4 \times 10^{-4}K^{-1}$, the temperature resolution can reach $1.0K$ theoretically. The optical resolution or the diffraction limit is calculated from the wavelength $\lambda = 532\,nm$ and numerical aperture $NA = 0.25$ with gives 1.1 μm. However, the light filed camera also limits the spatial resolution by the pixel size $p = 2.24\ \mu m$ and effective resolution ratio no more than 0.5. The spatial resolution of our system is determined to be $4.48\ \mu m$. For 3D light field imaging, other important characteristics are the depth resolution and depth of field. The depth resolution of the 3D TR system is calculated as $2.8\ \mu m$ and depth of field is $45\ \mu m$.

Though the R10μ light field camera takes 12-bit raw images, the SDK provided by Raytrix generates depth maps and total focus images in 8 bit depth. Hence an alternative has to be considered to achieve 12 bit depth reconstruction which is essential to resolve the TR signal. The following procedures shows how our alternative 12-bit data processing works:

(i) Take 5000 12-bit raw images for both heated and unheated target. The averaged unheated and heated raw images are carried out respectively;

(ii) Get an 8-bit image **D** to temporarily store the difference between the heated and unheated raw images;

(iii) Load image **D** into software as a new raw image. Combine with the depth map in generated by a separate 8-bit processing to finish the total focus process. The change of reflectance can therefore be calculated by back scaling.

The TR signal $(R - R_0)/R_0$ is obtained by this data processing procedure. With predetermined TR coefficients, we can evaluate the corresponding temperature change profile ΔT on the 3D surface.

2.5. Result and Discussion

A high power infrared $808\,nm$ laser diode using aluminium gallium arsenide (AlGaAs) as active layer and gallium arsenide (GaAs) as substrate was tested. The diode is mounted inside a 9mm TO can package. Figure 2.7 shows the images of the laser diode taken by the regular optical microscope, focusing on the semiconductor surface and the gold wire respectively. Figure 2.8 gives the 3D surface reconstruction via the light field camera, and the total focus image of the laser diode which is generated by focusing the raw image to the reconstructed depth map. Compared with the 2D images, 3D images obviously have an extended depth of view from light field cameras, while traditional 2D camera can only focus on a very small depth of field.

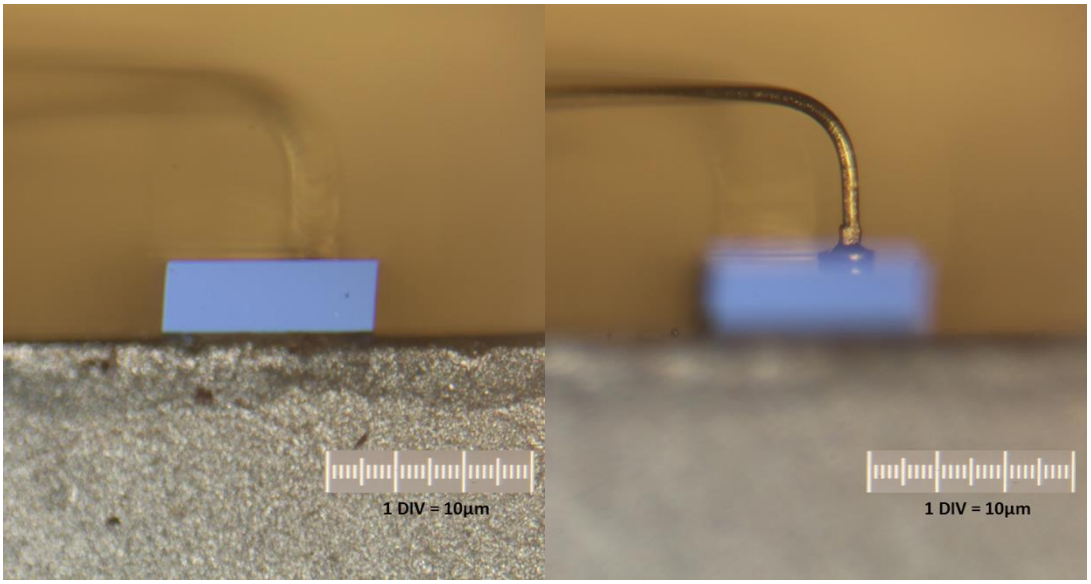

Figure 2.7 Two-dimensional (2D) microscope images of the laser diode. Width of the gallium arsenide (GaAs) surface is $300\ \mu m$; Diameter of the gold wire is $25\ \mu m$.

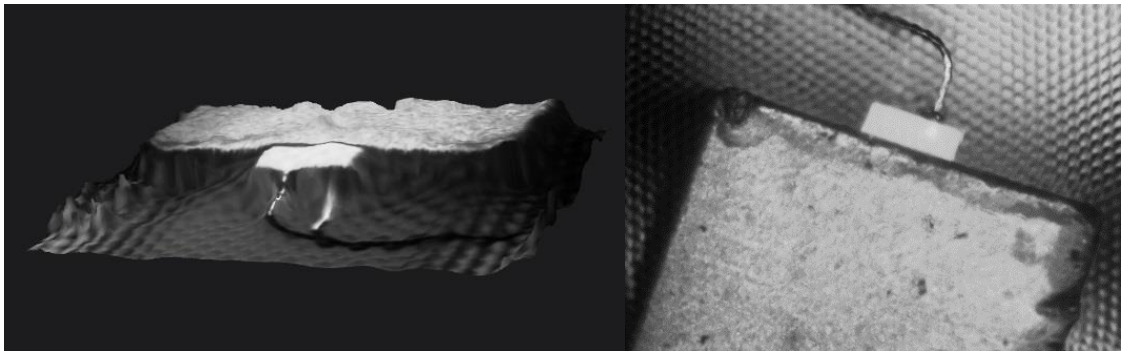

Figure 2.8 3D depth map and total focus image of $808\ nm$ laser diode. Width of the GaAs surface is $300\ \mu m$; Diameter of the gold wire is $25\ \mu m$.

First temperature measurement is conducted on the bright semiconductor surface. This surface is actually a polished end of the P-N junction which emits laser light. Images were taken both for unheated and heated conditions. The unheated images are taken under room temperature. The heated images are images of the laser diode when it is turned on and reaches steady state. The 12-bit data processing discussed above has been done

afterwards. Figure 2.9 is the profile showing the temperature change ΔT of the diode during operation. By observing the surface temperature change of the semiconductor, the expected high temperature region, i.e. the active layer locating close to the large heat sink, has been captured. Generally, the temperature distribution is relatively uniform on the surface when the laser diode reaches steady state. The surface temperature is comparable with the junction temperature of the laser diode, which is approximately $150\,℃$. The polished surface is flat so the incident angles should be almost the same everywhere. The edges of the surface have either too high or too low temperature change. This effect is induced by movement of the free-standing gold wires during heating, which bends and drags the semiconductor off its original location. This movement affects the raw images taken by the light field camera. Each micro-image has a slightly shift between heated and unheated conditions, which gives rise to the input error of the data processing.

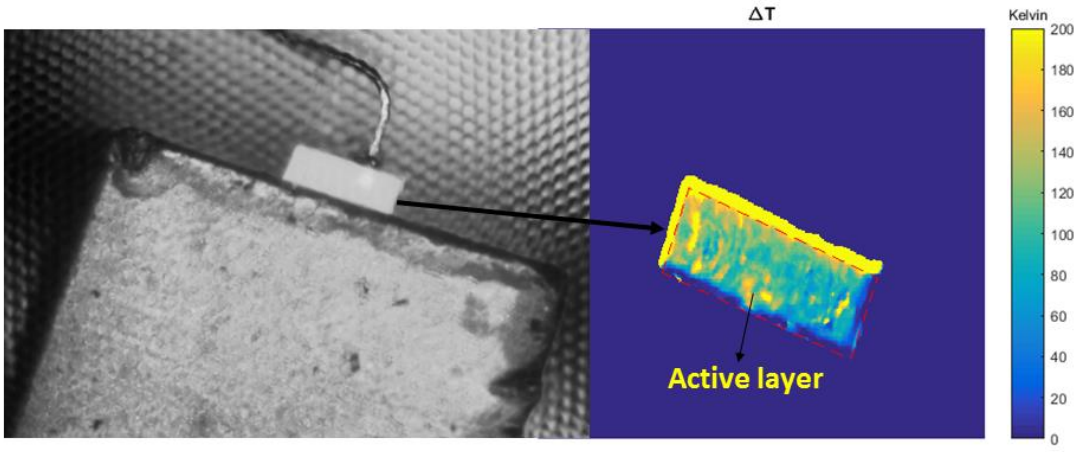

Figure 2.9 Temperature distribution on the semiconductor surface of the laser diode. The dashed line highlights the non-physical temperature measured due to the slight movement of the laser diode during heating. Width of the gallium arsenide surface is $300\ \mu m$.

The temperature of the gold wire is then measured to further show the benefit of 3D TR imaging. To get an enlarged image of the tiny gold wire (25 μm in diameter), the camera view lens is replaced by the 10X objective. A trade-off in this change is having larger magnification but less depth of field. Therefore, in the resultant images only a small depth range looks sharp. Measurement is done with $532\,nm$ green illumination. Refractive index of gold at wavelength $532\,nm$ is indicated by [96]:

$$n = 0.5446,\ k = 2.1406$$

Thermo-optic coefficient of gold can be obtained from [96]:

$$dn\ /\ dT = 4.2988 \times 10^{-4} K^{-1},\ dk\ /\ dT = -0.63718 \times 10^{-4} K^{-1}$$

Directional TR coefficients are then be evaluated by Equation (2.20).

The temperature profile of the gold wire based on 3D depth map has been presented in Figure 2.10. The temperature on a portion of the wire is presented since a sharp depth map is only valid in this small area with large magnification. If we look at the temperature distribution, high temperature appears in the locations which are in contact with the diode. This is true since the heating source in our test is the active layer inside the doped gallium arsenide semiconductor region.

Cross-sectional temperature distribution is quite uniform except the left and right edges. The reason that the left and right edges of the gold wire have a higher temperature value can be explained similar to the previous result in Figure 2.9. The target may not only shift in the x-y plane but also bends and rotates under the thermal expansion effect, so all micro-images projected by MLA move after heating. Subtraction of the averaged heated

raw image from the unheated raw image can induce unwanted errors. Hence, unlike the 2D TR imaging, imaging post-processing to compensate this movement can hardly be done in 3D case.

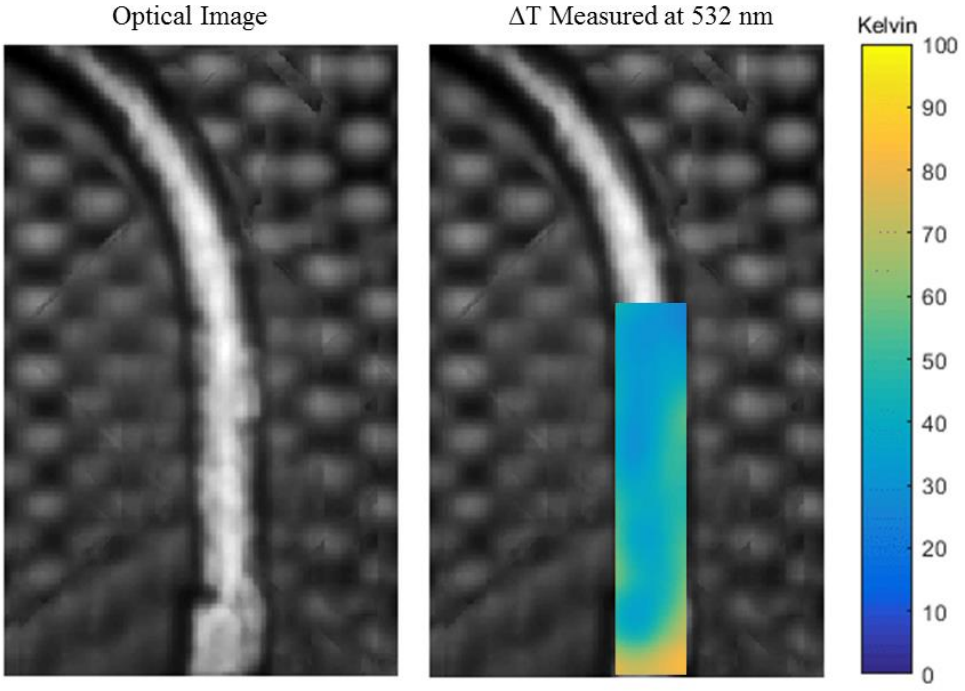

Figure 2.10 Total focus image of the gold wire and the temperature distribution measured at $532\ nm$. Diameter of the gold wire is $25\ \mu m$.

The uniform cross-sectional temperature distribution shows the advantage of our 3D TR imaging in resolving surface temperatures. In traditional 2D TR imaging, non-uniform temperature distribution along the cross-sectional direction of the 3D microstructure may occur [39] because of (i) target being out of focus at the curved edge of the wire in 2D images; (ii) inability to resolve directional reflectivity and its contribution in TR. Both (i) and (ii) caused inaccurate temperature measurement of the real 3D surface. Although current 3D TR imaging we just presented exists some problem,

especially regarding the thermal expansion effect, we've obtained convincing result to show the benefit of 3D TR thermography.

2.6. Summary

3D TR imaging techniques in measuring temperature distribution of microscale electronic devices with curved surfaces is introduced in this section. The expression of directional TR coefficient of common materials has been derived with arbitrary wavelength and incident angles. Data processing method has also been presented. The resultant thermal images indicate reasonable temperature profiles, benefits of extended depth of view and the ability to resolve reflecting directions. The imaging results show good temperature profile on most of the surface area of interest. However, some problems of current method and results need to be corrected. Thermal expansion of the target during heating process causes discrepancy between heated and unheated raw images and generates some non-physical temperature in certain region of the thermal image. The thermal expansion related movement issue can be solved by using two-wavelength TR method as explained in the next chapter.

.

3. TWO-WAVELENGTH THERMOREFLECTANCE IMAGING*

3.1. Motivation

Traditional single wavelength thermoreflectance (TR) techniques, relying on the comparison between optical images of a target with different temperatures, is very sensitive to the movement of target especially in the microscale cases. Thermal expansion of the target, as well as the associated movements, is the main limit of current TR technique despite of the advantages such as high spatial and temperature resolution. For example, planar movement of target due to thermal expansion can induce mismatching between the TR images from heated and unheated target. On the other hand, perpendicular movement of the target can cause image defocusing and make the recorded optical image blurred, which affects the accuracy of the microscale TR measurement. Moreover, miniature micro-electronic and micro-optical devices tend to have non-uniform amount of thermal expansion in different directions due to the presence of boundaries and different materials, which causes additional bending and rotation. The bending and rotation make the direct comparison between heated and unheated TR images even more challenging in

---

*Part of this chapter is reprinted with permission from (1) "Two-wavelength thermoreflectance and its application in temperature measurement of micro-electronic devices." by Zhang, Hongjie and Sy-Bor Wen. Proceedings of the ASME 2018 International Mechanical Engineering Congress and Exposition. Volume 8A, 2018. Copyright 2018 by ASME. (2) "Two-wavelength thermoreflectance in steady-state thermal imaging." by Zhang, Hongjie, Sy-Bor Wen and Arun Bhaskar. Applied Physics Letters 114, no. 15 (2019): 151902. Copyright 2019 by AIP Publishing.

traditional TR imaging with single wavelength illumination. Traditional TR imaging is mainly applied in quasi-steady-state temperature measurement with a lock-in scheme to reduce the signal-to-noise ratio. The modulated periodic heating can have the movement issues in TR imaging mitigated. An effort of compensating the thermal expansion was made by adding a piezoelectric position controller into the sample holder [97]. The reported system used real-time feedback control of a three-axis high precision piezoelectric stage to have the heated target always in focus on the CCD camera with similar positions. The reported method is a good way to compensate planar and perpendicular movement; however, it helps little in the case of possible bending and rotation of the target when it is heated. In this study, the first research objective is to develop a two-wavelength TR method in order to overcome the target movement issue due to thermal expansion.

3.2. Theory of Two-wavelength Thermoreflectance Imaging

In this study, a novel TR technique, namely, two-wavelength thermoreflectance (2WTR) imaging, is proposed to better handle the thermal expansion and the associated target movement issues during microscale TR temperature measurements.

In Section 2.3, TR equation and TR coefficient has been introduced and described in detail. When a second wavelength is considered in TR imaging, the following equation stands for both wavelengths.

$$R_i = (1 + \kappa_i \Delta T) R_{i0}, \qquad i = 1, 2 \tag{3.1}$$

Subscripts $i = 1, 2$ are applied in the equations corresponding to properties with wavelength λ_i. The ratio of the reflected light intensity R_1/R_2 can be approximated as following equation when $\kappa_i \Delta T$ is small:

$$R_1/R_2 = (R_{10}/R_{20})[1 + (\kappa_1 - \kappa_2)\Delta T] \tag{3.2}$$

R_{10}/R_{20} is the ratio of the reflected light intensity of the unheated target at wavelength λ_1 and λ_2, which may show spatial variations for each specific type of material if the illumination is not spatially uniform. If the quantity R_{10}/R_{20} is spatially uniform, and therefore can be replaced by a spatially independent constant in Equation (3.2), the distribution of R_1/R_2 will reflect the temperature distribution on the sample surface. Therefore, to use Equation (3.2) for determining two-dimensional (2D) surface temperature with the quantity R_1/R_2, the first step is to calibrate the TR experimental system to have uniform illumination shining on the target surface. The calibration procedure and result of uniform illumination will be presented after the description of 2WTR experimental setup.

There are at least two main advantages of introducing two wavelengths in TR imaging:

(i). Only the reflectance images of the target under heating conditions are required. However, in traditional single wavelength TR, TR signal relies on the comparison between heated and unheated reflectance images which is significantly affected by the thermal expansion of the target.

(ii). For some common materials such as gold, aluminum, titanium, etc., TR coefficient can be positive for certain wavelengths and negative for other wavelengths. When the two

wavelengths in two-wavelength TR are picked to have TR coefficients with opposite signs, the two-wavelength TR signal in Eq. (3.2) is increased compared with traditional single wavelength TR. This increased TR signal results in better temperature resolution and larger signal-to-noise ratio.

3.3. Experimental Setup and System Calibration

Figure 3.1 shows the 2WTR experimental setup adopted in this study. The system contains a digital micromirror device (DMD) type spatial light modulator (SLM) which allows us to calibrate the uniformity of illumination light intensity through an adaptive approach.

The 2WTR setup is mainly an optical system constructed with highly uniform illumination. The green and blue light-emitting diode (LED) light are first sent to the DMD type spatial light modulator. The DMD (Texas Instruments DLP4500) can fine tune the spatial distribution of the intensity of incoming light beam. Telecentric lens design is adopted to guide the light beam and form demagnified images. Bandpass spectral filters, with the center wavelength $470 \pm 2\ nm$ for blue illumination and $530 \pm 2\ nm$ for green illumination, are installed to narrow the bandwidth of illumination. Since the system operates with two different colors, all lenses in the system are achromatic doublet lenses to minimize the chromatic aberrations. An infinity-corrected microscope with a 20X $NA = 0.29$ apochromatic objective is adopted in the imaging optical design of two-wavelength TR imaging for microscale targets. A 16 bit depth grayscale CCD camera is the optical detector in the 2WTR system, which collects the reflected light signal through

the returning optical path. The triggering of LED and camera is synchronized by a digital input/output device (Measurement Computing USB1024LS).

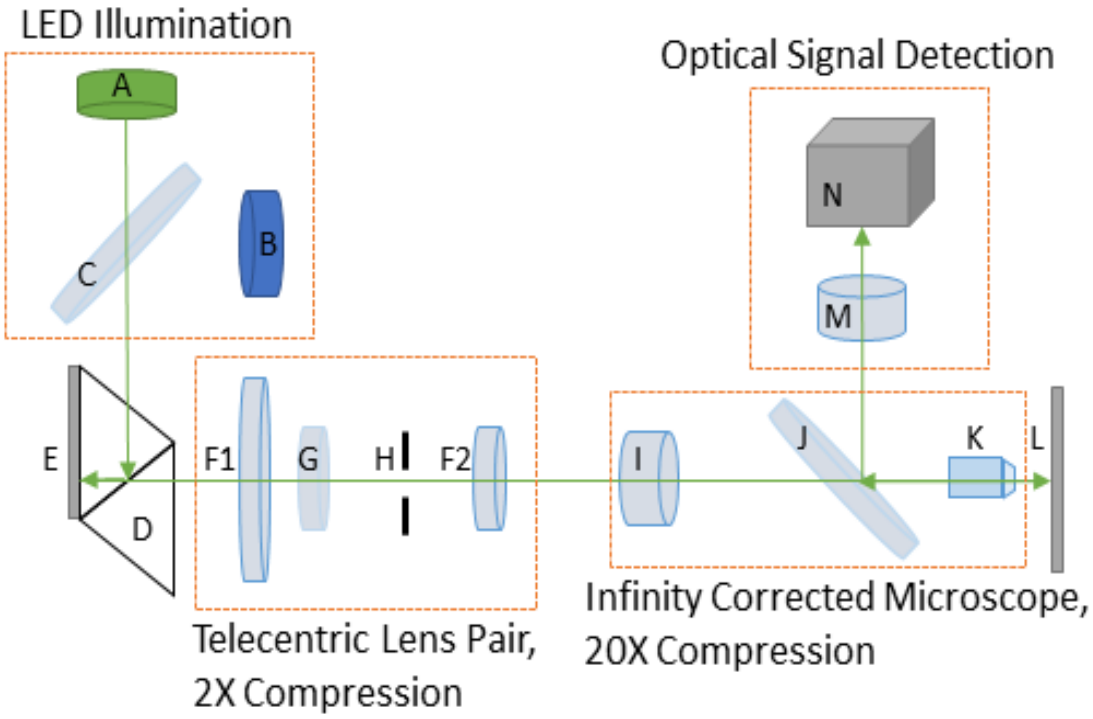

Figure 3.1 Schematic of the two-wavelength thermoreflectance (2WTR) imaging system. Only the green light rays are shown in the figure since blue ones follow a similar optical path. List of optics/elements: A. Collimated green light-emitting diode (LED) light; B. Collimated blue LED light; C. Dichroic mirror; D. Total internal reflection (TIR) prism; E. digital micromirror device (DMD) type spatial light modulator; F. (F1&F2) Telecentric lens pair with 2X image compression; G. Bandpass spectral filter; H. Aperture stop; I. Microscope tube lens; J. Beamsplitter; K. 20X apochromatic objective; L. Sample (Micro gold resistor); M. Tube lens; N. 16 bit depth CCD camera.

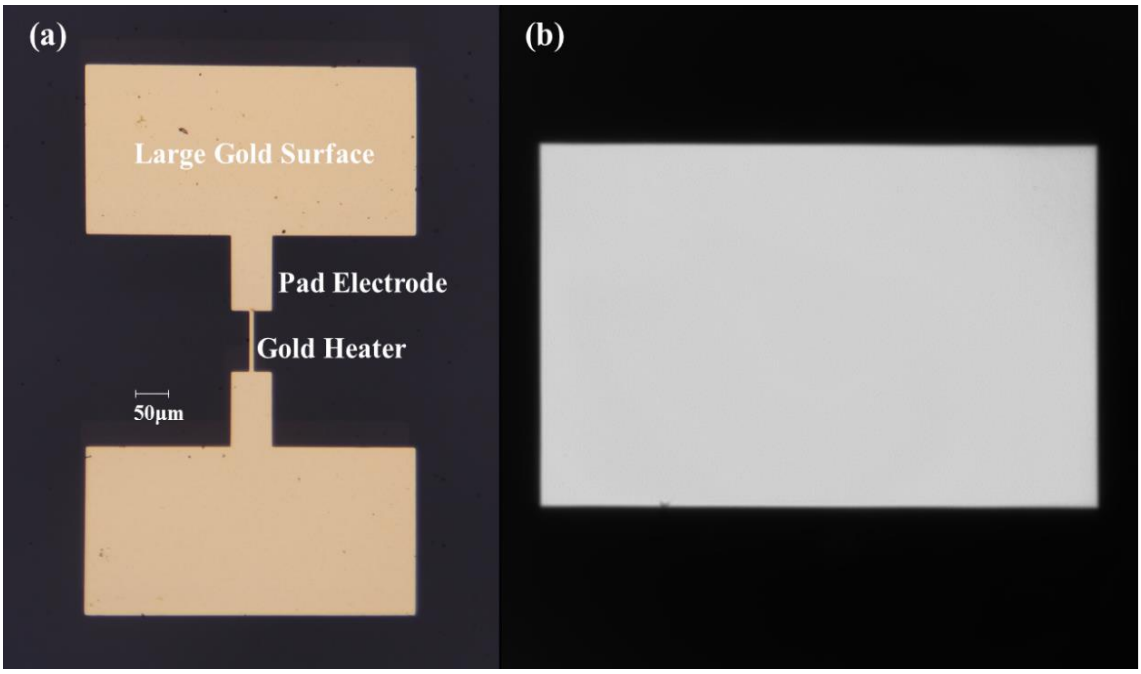

Figure 3.2 (a) Microscope image of the gold resistor; (b) Calibrated uniform illumination on a smooth gold surface.

In this study, steady-state surface temperature profile of a gold heater, as in Figure 3.2(a), is acquired by the described 2WTR system. The gold resistor is fabricated by a digital lithography system reported in [98]. The gold resistor has 100 nm thickness on the glass substrate. The gold resistor has a heater portion of 6 μm wide and 88 μm long. The pad electrode is 61 μm wide and 112 μm long. Silver conductive epoxy is applied to the large gold surface at the ends of the gold resistor. Compared with traditional single wavelength TR imaging, in which case the temperature of the sample is usually modulated by periodic heating, the gold resistor measured in the 2WTR system is supplied by a constant electrical current and steady-state temperature distribution is reached before measurement.

Illumination condition needs to be calibrated before the 2WTR experiment as discussed in previous paragraphs. In order to calibrate the uniformity of the illumination, a large area gold layer with the same thickness and surface condition of the gold resistor is placed in the current 2WTR system. Before the calibration is carried out, a one-to-one correspondence between DMD pixels and camera pixels are established by turning on some reference DMD pixels and finding their locations on the CCD image. The remaining pixel correspondence can be found based on interpolation. With the programmable capability of DMD type spatial light modulator (8 bit depth), the illumination is adjusted pixel by pixel through an iterative approach with the captured 16-bit CCD image similar to Newton's method in numerical analysis until reaching the desired light intensity. This procedure can provide a very uniform illumination, as shown in Figure 3.2(b). The calibration result with iterative scheme is presented in Figure 3.3 where the calibrated quantity R_{10}/R_{20} only has a spatial variation less than $\pm 0.8\%$.

Since the TR coefficient dependents on material surface condition, thickness, etc., calibration of TR coefficient is required for this thin gold micro-resistor. To calibrate the TR coefficient of the gold resistor, the glass plate, which is the base of the micro-resistor, is installed on a large Peltier heating stage. The surface temperature is monitored by a thermocouple. TR signals from the gold resistor with different temperatures are collected with the current 2WTR system. The TR coefficient of the gold resistor is determined as $3.03 \times 10^{-4} K^{-1}$ at wavelength $470\ nm$ and $-2.38 \times 10^{-4} K^{-1}$ at wavelength $530\ nm$. This result agrees with published values [99,100].

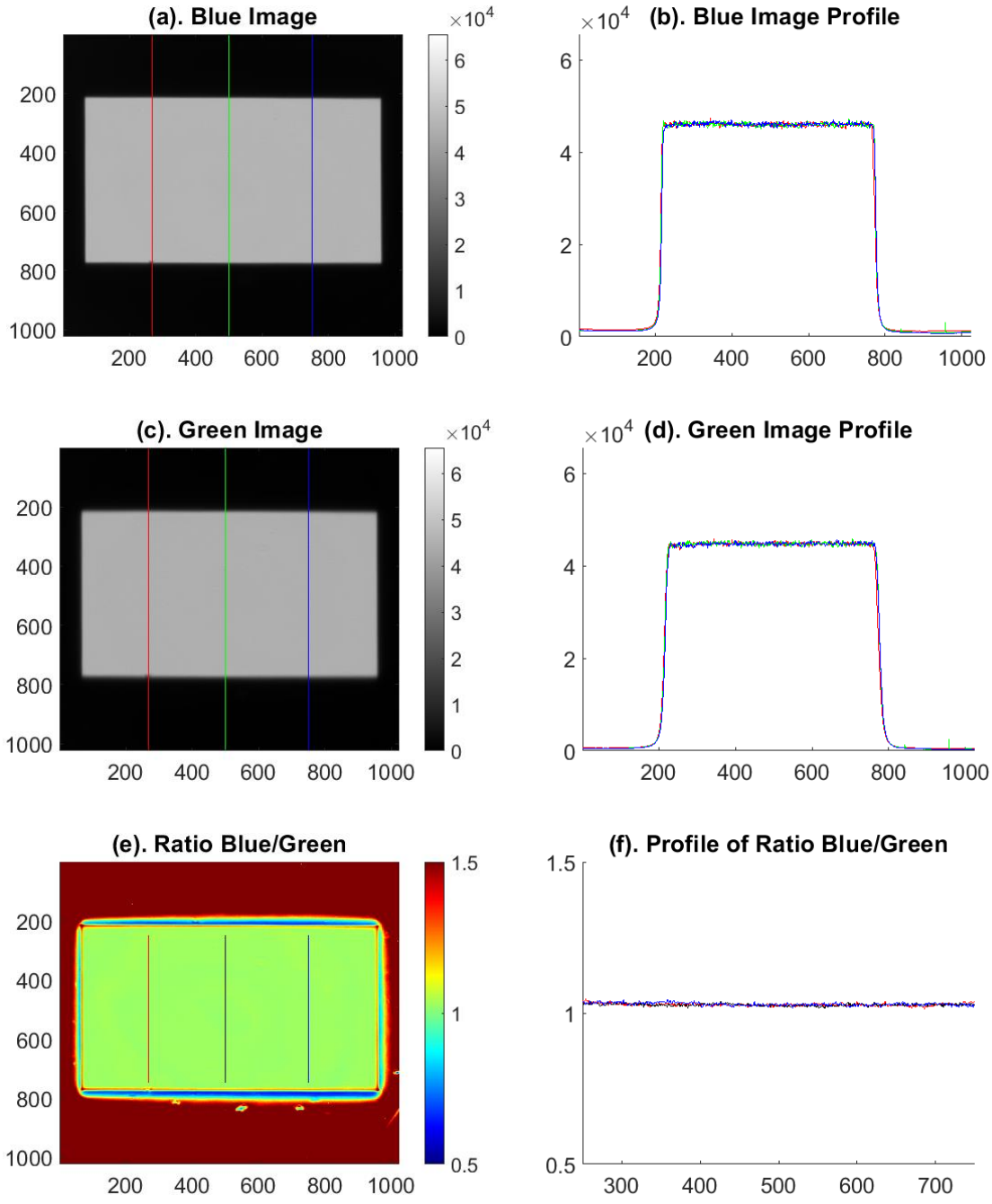

Figure 3.3 Calibration result of a large area gold layer illuminated with blue 470 nm and green 530 nm illumination through an iterative scheme (after 6 iterations). (a). Image of the gold layer with blue illumination; (b). Intensity profile on three vertical lines in the blue illuminated image; (c). Image of the gold layer with green illumination; (d). Intensity profile on three vertical lines in the green illuminated

image; (e). Contour of quantity R_{10}/R_{20}; (f). Profile on three vertical lines in the contour of quantity R_{10}/R_{20}.

The temperature resolution of current 2WTR system is mainly limited by the bit depth of DMD and the resulting spatial illumination uniformity. By doing error analysis of Equation (3.2), the temperature resolution of current 2WTR system is $15\ K$. Note that with higher bit-depth DMD (e.g., commercially available 12-bit models), the temperature resolution could be better than $1\ K$ based on current 2WTR experimental scheme.

The optical resolution OR is calculated from the wavelengths $\lambda_1 = 470\ nm$, $\lambda_2 = 530\ nm$ and numerical aperture of the 20X objective lens $NA = 0.29$,

$$OR = \max\left(\frac{\lambda_1}{2NA}, \frac{\lambda_2}{2NA}\right) = 0.91\ \mu m \tag{3.3}$$

Digital resolution DR is determined by the CCD pixel size $p = 5.5\ \mu m$ and microscope magnification ratio $M = 20$,

$$DR = \frac{p}{M} = 0.28\ \mu m \tag{3.4}$$

As a result, the system spatial resolution is determined by the diffraction limit which is $0.91\ \mu m$.

3.4. Result and Discussion

The steady-state surface temperature profiles of the heated gold resistor under different currents are measured with the 2WTR system. Figure 3.4 presents the measurement results of the gold resistor by two-wavelength TR when (a) $32\ mA$ (b) $42\ mA$, and (c) $53\ mA$ currents are supplied. Previous studies on the TR temperature

measurement of similar gold resistors can be found [38,101]. One of the main advantages of the 2WTR method over traditional single wavelength TR is that thermal expansion does not affect 2WTR temperature measurement. Figure 3.4(d) gives traditional single-wavelength TR measurement of the gold resistor under $42\ mA$ current without image post-processing. The images of the heated and unheated gold resistor are compared directly in this case. Due to the fact of image mismatching between the heated and unheated conditions, there are non-physical temperature values appearing along the edges as well as the defects regions of the gold resistor. Image post-processing, including image scaling, translation and rotation, can be done. However, it is not reasonable when the sample experiences bending or rotation in three-dimensional space. Also, image post-processing can significantly increase noise level in the final temperature measurement, as shown in Figure 3.4(e) when a $42\ mA$ current is supplied. Meanwhile, 2WTR, by getting the temperature distribution solely from the heated condition, as shown in Figure 3.4(b) with the same current condition, generate fewer non-physical temperature values along the edges of the gold resistor compared with Figure 3.4(d) and smaller noise level compared with Figure 3.4(e). The measurement error on the edges of the gold resistor in 2WTR can be attributed to chromatic effect and three-dimensional structure of the gold resistor that cause different light diffractions for different colors even though the incident light is highly uniform.

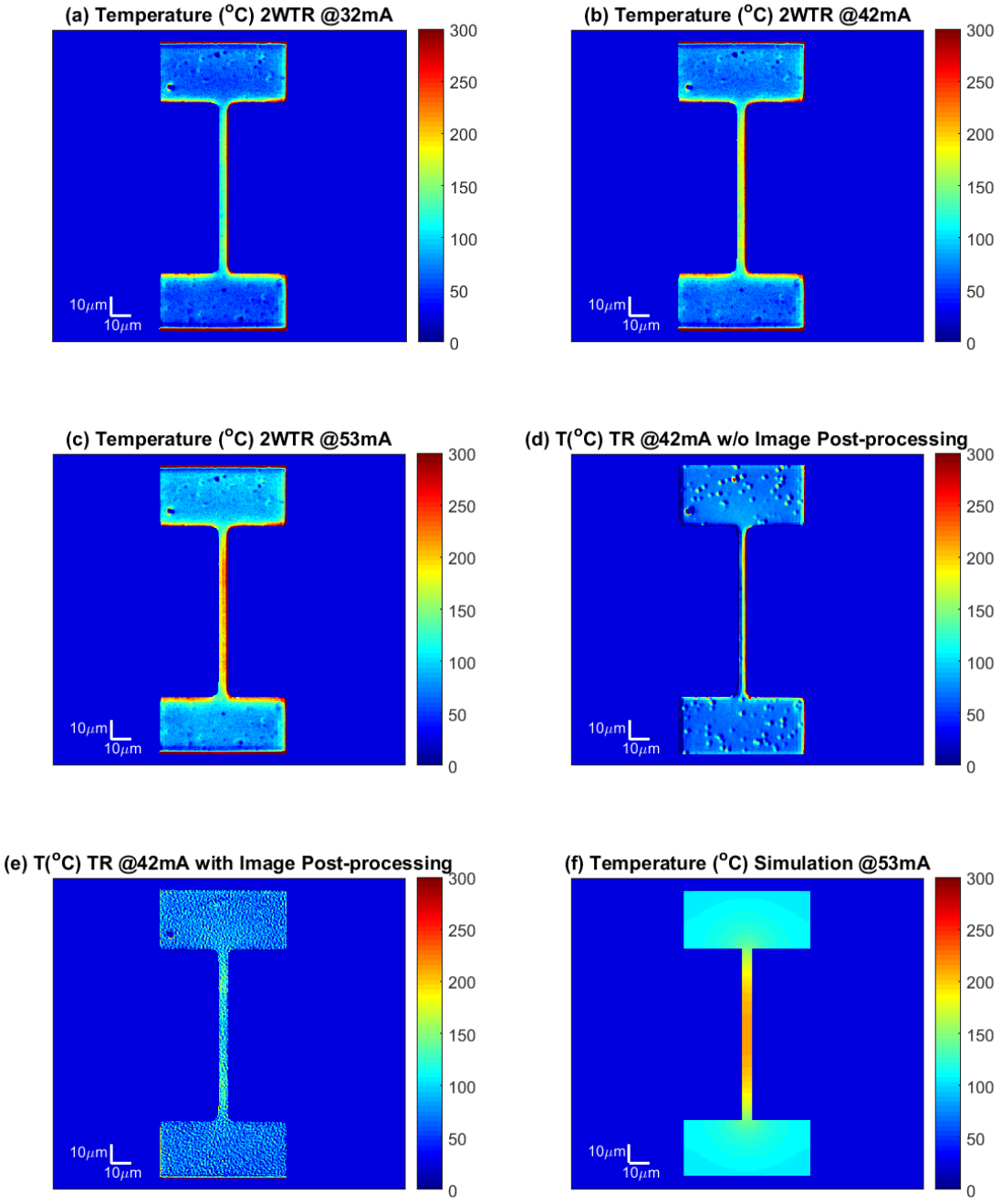

Figure 3.4 2WTR temperature measurement of the gold resistor under a current of (a). 32 mA, (b). 42 mA, (c). 53 mA; Single wavelength thermoreflectance (TR) temperature measurement of the gold resistor under a current of 42 mA (d). with direct image subtraction; (e). with image post-processing to match heated and unheated images; (f). Corresponding heat transfer simulation result the temperature profile of the gold resistor under a current of 53 mA.

The other advantages of 2WTR is that 2WTR method provides a higher TR signal than the traditional single wavelength TR method. The TR signal of 2WTR is $(\kappa_1 - \kappa_2)\Delta T$. The two TR coefficients of gold at the two adopted wavelengths have the opposite sign, which provide about two times stronger TR signal. Actually, for some common materials such as gold, aluminum, titanium, etc., TR coefficient can be positive in certain wavelength range and negative in others. When the two optical wavelengths adopted are appropriately selected, the increased TR signal of 2WTR over single wavelength TR provides better sensitivity and higher temperature signal-to-noise ratio.

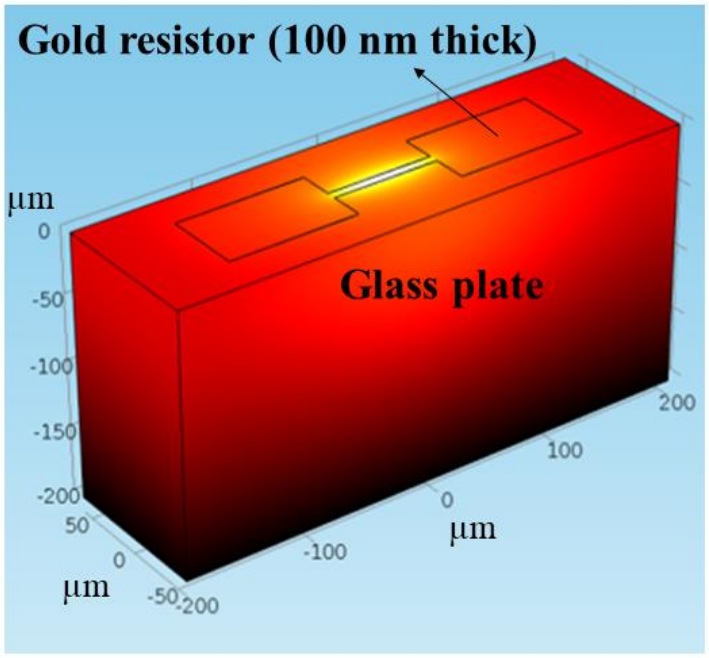

Figure 3.5 Simulation domain of the steady-state heat transfer simulation of the microscale gold resistor on a glass plate.

For further comparison, heat transfer simulation of the gold resistor has been obtained from solving steady-state heat diffusion equation with corresponding Joule heating ($53\,mA$ constant current) and boundary conditions. The simulation domain is shown in Figure 3.5. In simulation, the property parameters specified include thermal conductivity of gold $k_{gold} = 315\,W/mK$, thermal conductivity of glass $k_{glass} = 0.7\,W/mK$ and heat convection coefficient $h_{conv} = 15\,W/m^2K$. The dimensions of the gold resistor given previous paragraphs are also included in the simulation. The temperature profile obtained by simulation is given in Figure 3.4(f). Compared with Figure 3.4(c), the difference between the two profiles are within the temperature resolution of current 2WTR system.

3.5. Summary

In this chapter, a two-wavelength thermoreflectance (2WTR) imaging technique is presented. The 2WTR system, with the capability of programmable blue and green illumination, is first calibrated to have highly uniform illumination (determined by the bit depth of the spatial light modulator). The 2WTR method and system are validated by measuring steady-state surface temperature distribution of a microscale gold heater under different currents after TR coefficients of the gold resistor at wavelength $470\,nm$ and $530\,nm$ are determined. The measured temperature profiles agree well with previous studies and simulation results. 2WTR obtains temperature information from heated target under operation directly, hence is not affected by the movement of the target induced by thermal expansions. 2WTR also provides a higher TR signal than traditional TR when the

two adopted wavelengths are appropriately selected to have opposite signs. 2WTR, as the proposed thermal imaging technique, is valuable in measuring temperature of operating micro-electronic and micro-optical devices without been affected by the movement of the target mainly due to thermal expansion. The obtained steady-state temperature measurement is valuable in thermal management of micro electrical/optical devices.

4. LIGHT FIELD PROJECTION AND PHOTOLITHOGRAPHY*

4.1. Motivation

The existing three-dimensional (3D) photolithography techniques have been reviewed in Section 1.3. Stereolithography is a stable and maskless method applied for 3D printing. However, the layer-by-layer additive process limits manufacturing throughput and struggles fabricating free standing patterns. Holographic lithography is a high-throughput method, but the spatial resolution of 3D patterning suffers from the speckles resulting from the interference of different reflected portions of the incident beam with random relative optical phases. Single spot multi-photon photolithography has the highest spatial resolution down to sub-diffraction-limit. However, involving point-by-point scanning to pattern a 3D structure is time consuming.

Based on the fact that a 3D projection and photolithography technique which can pattern 3D microscale structures with fast speed (single projection) and high resolution (hundreds of nm) has not been reported in the literature, a new microlens array (MLA) based system with the capability of projecting satisfactory 3D microscale patterns and allowing submicron photolithography in the future is designed and developed in this study.

This research is inspired by the 3D thermoreflectance (TR) imaging described in Chapter 2, which uses MLA based light field camera as an optical detector. The new 3D projection and photolithography system can be considered as an inverse operation of light field camera. In light field imaging/camera, one point on the main object is imaged by charge-coupled device (CCD) pixels beneath multiple microlenses. In the new 3D projection and photolithography system, CCD sensors are replaced with a programmable spatial light modulator (SLM) which can control the spatial and intensity distribution of light beam. By properly control the pixels on the SLM, including their on-off status and intensity, multiple light beams passing through different microlenses converge to a small voxel in the 3D space. With a pixel value map of SLM, a group of voxels that forms a 3D structure can be projected simultaneously. The projection system, after validation, is then be utilized to perform 3D single photon photolithography. Since the new 3D projection and photolithography technique originates from light field imaging, it is named light field 3D projection and photolithography.

4.2. Design of Light Field Three-dimensional Projection and Photolithography

Light field 3D projection can be considered as an inverse operation of light field imaging, which is an integral imaging technique for capturing 3D images. The optical design of light field 3D projection is illustrated in Figure 4.1. The idea is to place a MLA at distance d away from a SLM. In order to control how the light beams from the programmable SLM pixels are refracted on each microlens, light beams parallel to the

optical axis is preferred and designed. Ray tracing scheme to determine on/off values of SLM pixels in order to reconstruct desired 3D virtual structures needs to be developed.

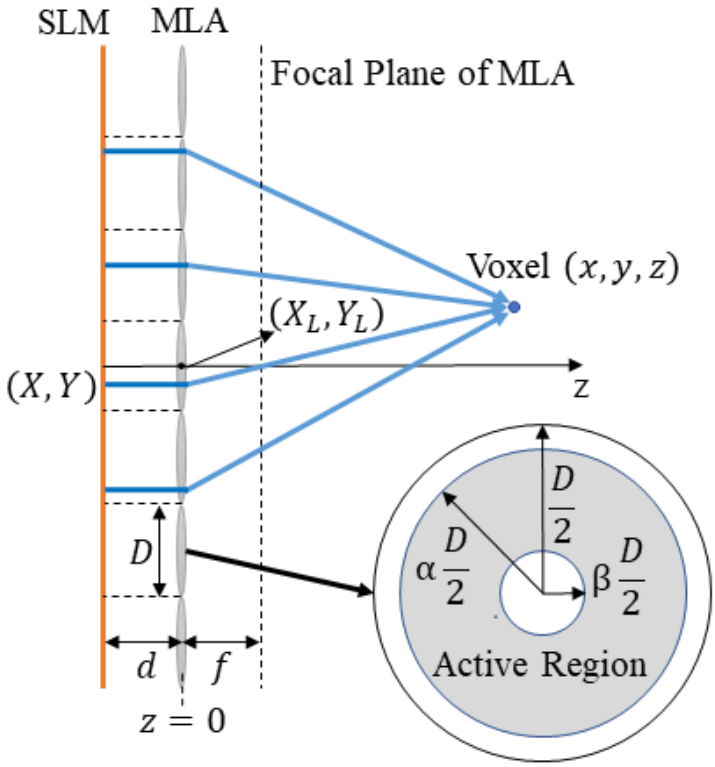

Figure 4.1 Ray tracing to determine the required spatial light modulator (SLM) pixels at position (X, Y) to be turned on for projecting one voxel at (x, y, z). D is the pitch size of microlens array (MLA), f is the focal distance of each microlens; (X_L, Y_L) is the center location of each microlens. Active region of SLM beneath each microlens illustrated with gray shading having parameters $0 \leq \beta < \alpha \leq 1$.

The MLA has pitch size D and focal distance f. A Cartesian coordinate system is set up with plane $z = 0$ placed on the surface of the MLA. The centers of microlenses are denoted by (X_L, Y_L). For a designed voxel (x, y, z) to be projected in the 3D space after MLA, the corresponding SLM pixels (X, Y) to be turned on are

$$X = X_L - \frac{f}{z-f}(x - X_L) \tag{4.1}$$

$$Y = Y_L - \frac{f}{z-f}(y - Y_L) \tag{4.2}$$

To reduce the focused voxel size and to avoid the usage of microlens boundaries, only SLM pixels within the active region of each microlens is used. The active region of a microlens is defined by two parameters α and β as demonstrated in Figure 4.1 with $0 \leq \beta < \alpha \leq 1$. The microlens parameter α determines the outer boundary of active region and limits the use of outer portion of each microlens, while the microlens parameter β determines the inner boundary of active region and limits the use of center portion of each microlens. Limited number of microlenses and associated pixels of SLM can be used in projecting each voxel (x, y, z) of a designed 3D structure. SLM pixels beneath a microlens centered at (X_L, Y_L) can only be turned on when the following condition is satisfied:

$$\beta \frac{D}{2} \leq \sqrt{(X - X_L)^2 + (Y - Y_L)^2} \leq \alpha \frac{D}{2} \tag{4.3}$$

Microlenses centered at (X_L, Y_L) that have Equation (4.3) stand are called active microlenses. By substituting Equations (4.1) and (4.2) into Equation (4.3), an active microlens should have

$$\frac{\beta D(z-f)}{2f} \leq \sqrt{(X_L - x)^2 + (Y_L - y)^2} \leq \frac{\alpha D(z-f)}{2f} \tag{4.4}$$

If the corresponding pixel beneath each active microlens is turned on, the multiple parallel beams after being refracted from the active microlenses have the only intersection point (x, y, z), which is the intended projection voxel. The projection voxel has the highest intensity in the 3D space nearby as if lights are focused onto this point. By performing

such projection of multiple voxels in the 3D space after MLA, a 3D virtual structure can be established.

Hence, we can achieve 3D light field projection in the following manner:

(i). First, discretize the designed 3D structure that is intended to project into a projection voxel cloud;

(ii). Second, for each voxel of the voxel cloud, find the active microlenses via Equation (4.3) and corresponding pixels that need to be turned on through ray tracing, i.e. Equation (4.1) and (4.2);

(iii). Third, generate a pixel value map, or elemental images, that contains all the corresponding pixels with intensity values adjusted. The pixel value map becomes the system input to the SLM.

4.3. Experimental Setup and System Calibration

A light field 3D projection/photolithography system is constructed to achieve the optical scheme described above. A stable blue light-emitting diode (LED) with center wavelength $450\,\mu m$ acts as the light source of a SLM (Texas Instruments DLP LightCrafter 4500) through a total internal reflection (TIR) prism. The digital micromirror device (DMD) type SLM can adjust the intensity distribution of incident light beam by turning micromirrors on or off. The programmable SLM can provide spatially distributed illumination with 8 bit depth digital intensity variation.

MLA (Edmund Optics 86-745) with focal distance $f = 4.8\,mm$ and pitch $D = 300\,\mu m$ is used in this study. Rather than providing the pixel value map of SLM directly

before the MLA, an optical relay is applied to bring the pixel value map to the entrance of MLA. Separation distance between the relayed image of SLM and the MLA $d \approx 2.4\,mm$. The optical relay is essentially a telecentric lens pair with two achromatic doublet (both focal distances $100\,mm$) sepearted by $200\,mm$. The optical relay makes the distance control between the pixel value map and the MLA easier during the coupling process. A spatial filter is installed in the optical rely to limit the divergence angle of the light beams towards the MLA. By reducing the size of opening of the aperture stop, light beams sent from the relayed image of SLM toward the MLA can be not only narrow, but also nearly parallel to the optical axis of the whole optical system.

The orange box in Figure 4.2 which consists of the SLM and MLA combination has been described in detail in Section 4.2. With the designed optical scheme, a 3D virtual structure is reconstructed in the 3D space after the MLA through a correct pixel value map from the SLM.

A microscope telecentric lens pair consisting of a tube lens (focal distance $200\,mm$) and a 16X, numerical aperture (NA) 0.8, objective lens (Nikon 16X CFI LWD Plan Fluorite) is adopted to compress the macroscale 3D virtual structure to microscale. In the associated light field 3D photolithography, the compressed 3D virtual structure is projected into permanent epoxy negative photoresist, e.g. SU-8 2150, coated on a silicon wafer. The exposed photoresist becomes cross-linked while the unexposed part remains soluble to SU-8 developer. A beam-splitter is inserted in the optical path of the telecentric lens pair to guide the reflected image from the sample into a CCD camera, which can real-time inspect the projected patterns.

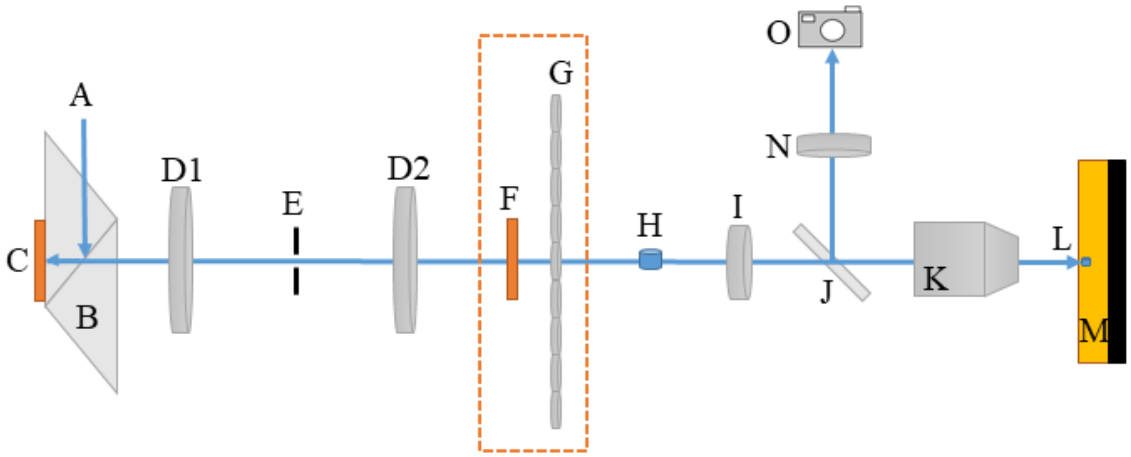

Figure 4.2 Configuration of the light field three-dimensional (3D) projection/photolithography system. List of elements: A. Collimated light-emitting diode (LED) light with 405 nm center wavelength; B. Total internal reflection (TIR) prism; C. Digital micromirror device (DMD) type SLM; D. (D1&D2) Telecentric lens pair; E. Aperture stop with minimum opening; F. Relayed image of SLM; G. Microlens array (MLA); H. Reconstructed 3D pattern; I. Microscope tube lens; J. Beamsplitter; K. 16X objective lens; L. Compressed 3D pattern; M. SU-8 2150 negative photoresist layer on a silicon wafer; N. Tube lens for imaging; O. Grayscale charge-coupled device (CCD).

A pixel value map of SLM, which is a map showing on/off status and intensity of each micromirror for projecting a desired 3D virtual structure through MLA, is illustrated in Figure 4.3. The pixel value map contains different facets of the 3D virtual structure to be projected through each microlens.

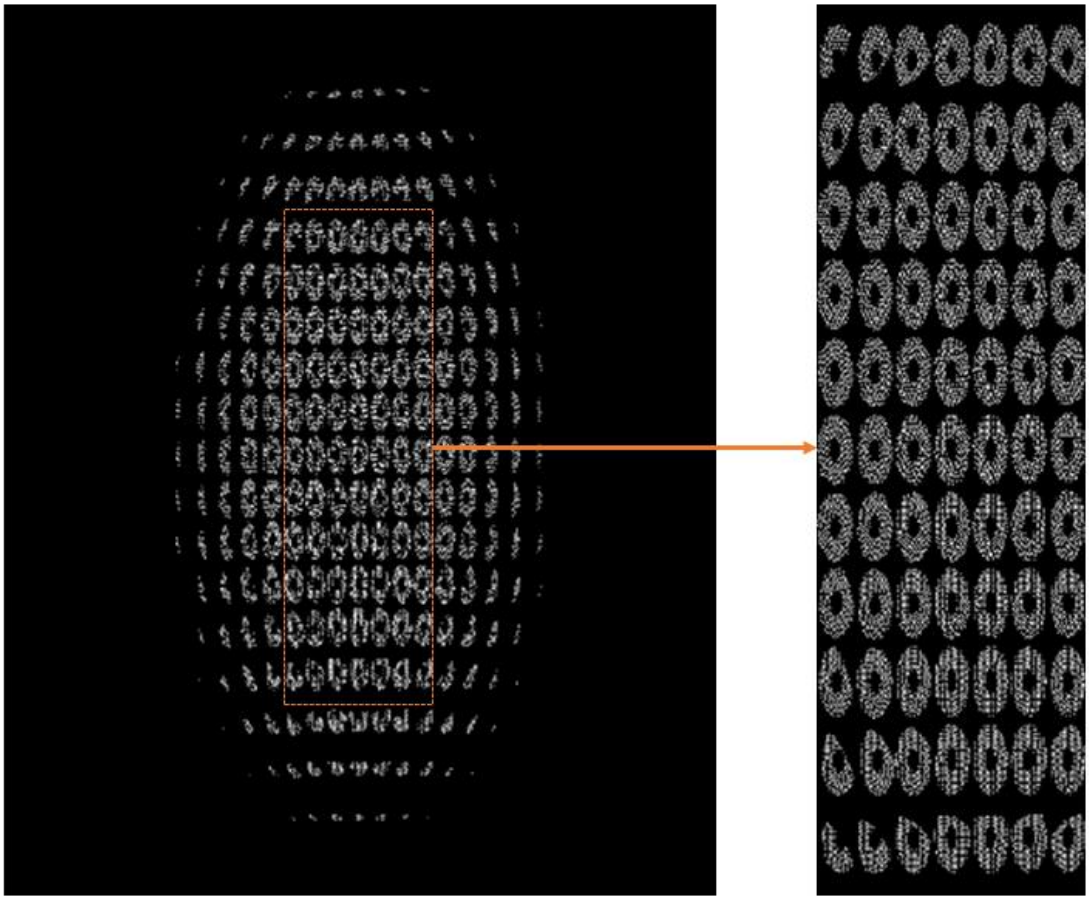

Figure 4.3 A pixel value map displayed by SLM in order to project a 3D cone surface. Center portion of the pixel value map is enlarged.

A successful 3D virtual structure reconstruction with the proposed light field 3D projection relies on a precise determination of the relative positions between each SLM pixel and each microlens of the MLA. Generally speaking, the correspondence is unknown after the system is set up. Therefore, an experimental calibration to determine the relative positions is required. The calibration starts from setting all SLM pixels at maximum intensity (solid field) and focusing the camera on the MLA plane where a sharp image of the MLA boundaries, i.e. common edges of adjacent microlenses, can be observed. The

image shown in Figure 4.4(b) gives the locations of MLA boundaries in the camera space. Then a set of short straight lines, as showed in Figure 4.4(c), at various SLM locations is tested for each MLA boundary. When these straight-line patterns are projected, the resultant images captured by the camera, which look like Figure 4.4(d), are examined at the MLA boundary locations indicated by Figure 4.4(b). MLA boundaries appear brightest when the projected straight lines exactly overlap with MLA boundaries. As a result, a mapping function between all SLM pixels and microlens locations can be obtained with given SLM pixel size and MLA pitch size.

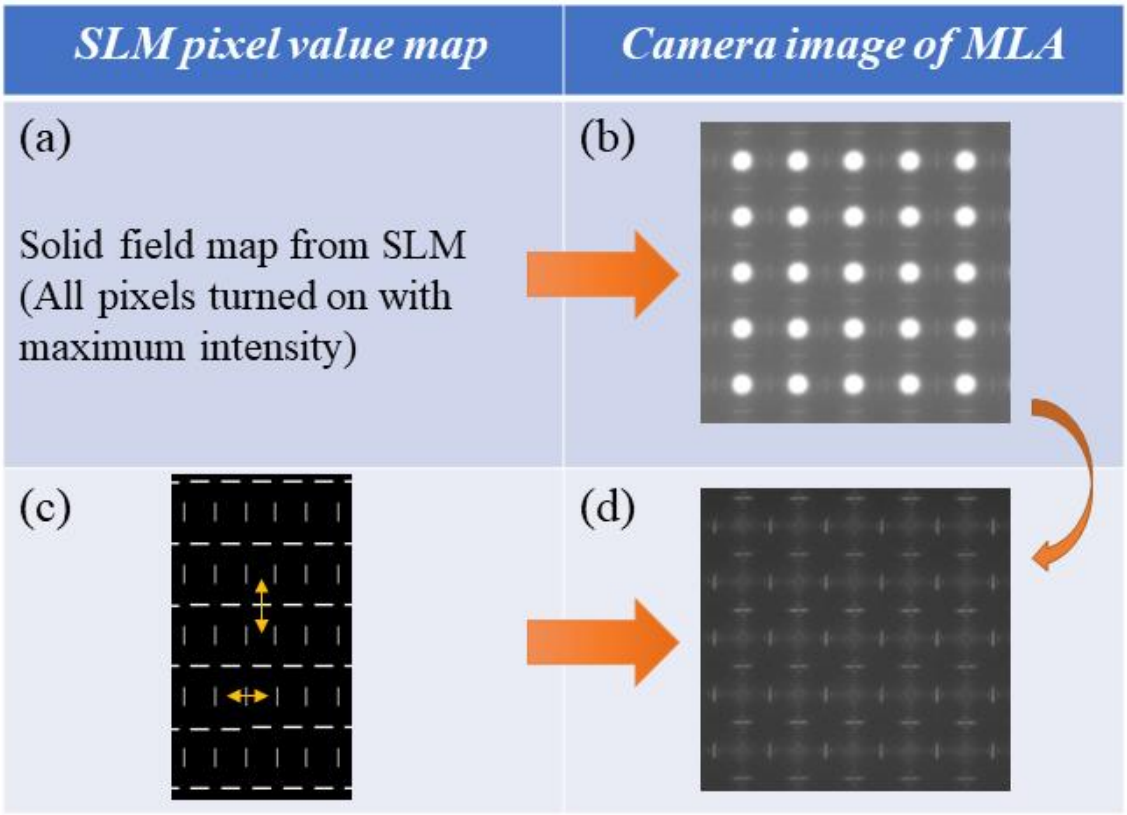

Figure 4.4 Flow chart of MLA-to-SLM calibration: (b). Image of MLA showing the sharp edges of microlens boundaries when full background illumination is turned on; (c). Test pixel value map to be projected in order to find the microlens boundary locations on SLM; (d). Image of MLA when the test pixel value map is projected.

4.4. Study of System Lateral and Depth Resolution

To study the lateral and depth resolution of the light field 3D photolithography system, consider a voxel on the optical axis of a microlens for simplicity, i.e. $x = y = 0$ with the coordinate system defined in Figure 4.1. For a microlens centered at (X_L, Y_L), define the microlens distance index i by the following equation:

$$\sqrt{X_L^2 + Y_L^2} = iD \tag{4.5}$$

The microlens distance factor i represents how far away the active microlens of interest is from the center microlens at position $(0,0)$. In a 2D square-shaped MLA, the possible values of microlens distance factor i are from the series $I = \{\sqrt{j^2 + k^2}\} = \{0,1,\sqrt{2},2,\sqrt{5},\cdots\}$, where j, k are integers. As a result, Equation (4.4) can be rewritten with respect to i

$$\frac{\beta(z-f)}{2f} \leq i \leq \frac{\alpha(z-f)}{2f} \tag{4.6}$$

Number of rays, or number of active microlenses, reflects the number of corresponding pixels for a voxel projected at depth z. Number of rays is equivalent to the number of i values from series I that satisfy Equation (4.6). Figure 4.5 shows how number of rays is related to the projected voxel at different depths, with MLA focal distance $f = 4.8\ mm$ and pitch $D = 300\ \mu m$. Generally, number of rays increases when depth of voxel z increases. Active region parameter α is selected to first avoid the usage of microlens boundaries, and second reduce the discrepancy in number of rays for voxels at different

depth on the 3D surface. The intensity of resultant pixel value map which should be adjusted proportionally in consideration of similar voxel intensity on the 3D projection surface. Active region parameter β is selected by taking depth resolution into account. When β is a nonzero number, the center portion of each microlens is blocked. Therefore, the angle of rays converging to a voxel is increased, which results in an improved depth resolution. This will be discussed in detail in the depth resolution analysis next. The active region parameters we select for light field 3D projection/photolithography system is $\alpha = 0.3$ and $\beta = 0.9$. The number of rays for a voxel under this condition is given in Figure 4.5(c).

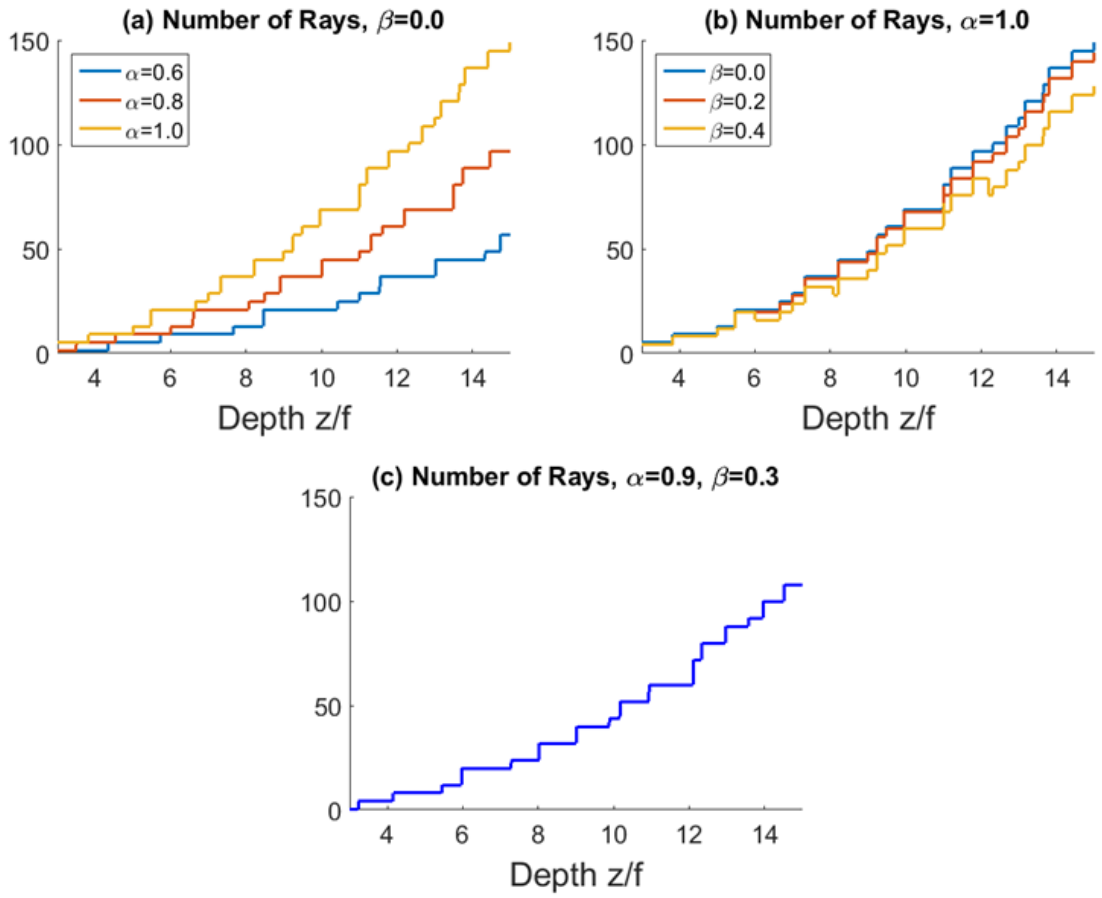

Figure 4.5 Number of rays corresponding to one voxel at different depths in the light field 3D projection/photolithography system. MLA focal distance $f = 4.8\,mm$ and pitch $D = 300\,\mu m$. (a). Number of rays when microlens active region parameter $\beta = 0$, i.e. all center portion of microlenses is active, α values vary; (b). Number of rays when microlens active region parameter $\alpha = 1$, i.e. all outer portion of microlenses is active, β values vary; (c). Number of rays when microlens active region parameter $\alpha = 0.9, \beta = 0.3$.

4.4.1. Lateral Resolution

Optical lateral resolution of the light field 3D projection system can be estimated by the numerical aperture of the optical system. The light rays with largest angle converging to a voxel is θ_R

$$\tan\theta_R = \frac{\alpha D}{2f} \tag{4.7}$$

After the microscope compression with magnification ratio M $(M > 1)$, the light rays with largest angle in microscale projection is increased to θ_{proj}

$$\tan\theta_{proj} = M\tan\theta_R \tag{4.8}$$

The optical lateral resolution can therefore be expressed via numerical aperture $\sin\theta_{proj}$

$$OR_L = \frac{\lambda\sqrt{M^2\alpha^2D^2 + 4f^2}}{2M\alpha D} \tag{4.9}$$

For wavelength $\lambda = 405\,nm$, magnification $M = 16$, MLA focal distance $f = 4.8\,mm$ and pitch $D = 300\,\mu m$, and active microlens parameter $\alpha = 1$, optical lateral resolution of system $OR_L = 453\,nm$.

Regarding the digital lateral resolution, the smallest lateral voxel size is limited by two factors: (i). The finite size of SLM pixel s; (ii). The finite size of aperture stop opening (spatial filter) in the first telecentric lens pair cause light sent from each SLM pixel has an angle of divergence θ.

The extent near the designed projection voxel due to finite size of SLM pixel s, is Δx in Figure 4.6(a).

$$\Delta x = \frac{s(z-f)}{f} \tag{4.10}$$

The effect of angle of divergence is dependent on the configuration of the light field 3D projection system. When separation distance between the relayed image of SLM and the MLA d is greater than MLA focal distance f, real image of each pixel is formed on the other size of MLA, as shown in Figure 4.6(b) and (c); When $d = f$, parallel beams form

after being refracted from MLA, as shown in Figure 4.6(d); When $d < f$, virtual images of SLM pixel is formed on the left of MLA, light beams are diverging after being refracted from MLA, as shown in Figure 4.6(e). In all cases, the following relation stands,

$$\delta x = 2d \tan\theta \left| 1 - \frac{z(d-f)}{fd} \right| \tag{4.11}$$

The digital lateral resolution of the light field 3D projection system after microscope compression is

$$DR_L = \frac{1}{M}(\Delta x + \delta x) \tag{4.12}$$

Similar to light field camera, each configuration of SLM and MLA combination performs different at different depth. Especially for the configuration $d > f$, voxel size can be smallest when light beams after MLA are converging. As shown in Figure 4.7, although the configuration $d = 1.1f$ is not the best at certain depths, it has an overall better performance in the whole depth range $[3f, 15f]$. The system parameters used are MLA focal distance $f = 4.8\,mm$,pitch $D = 300\,\mu m$, angle of divergence $\theta = 0.6°$ and SLM pixel size $s = 10.8\,\mu m$. Obviously, the system digital lateral resolution is one order greater than the optical lateral resolution. Hence the smallest lateral voxel size is determined by the digital lateral resolution DR_L, which can be <10 μm in a large depth range.

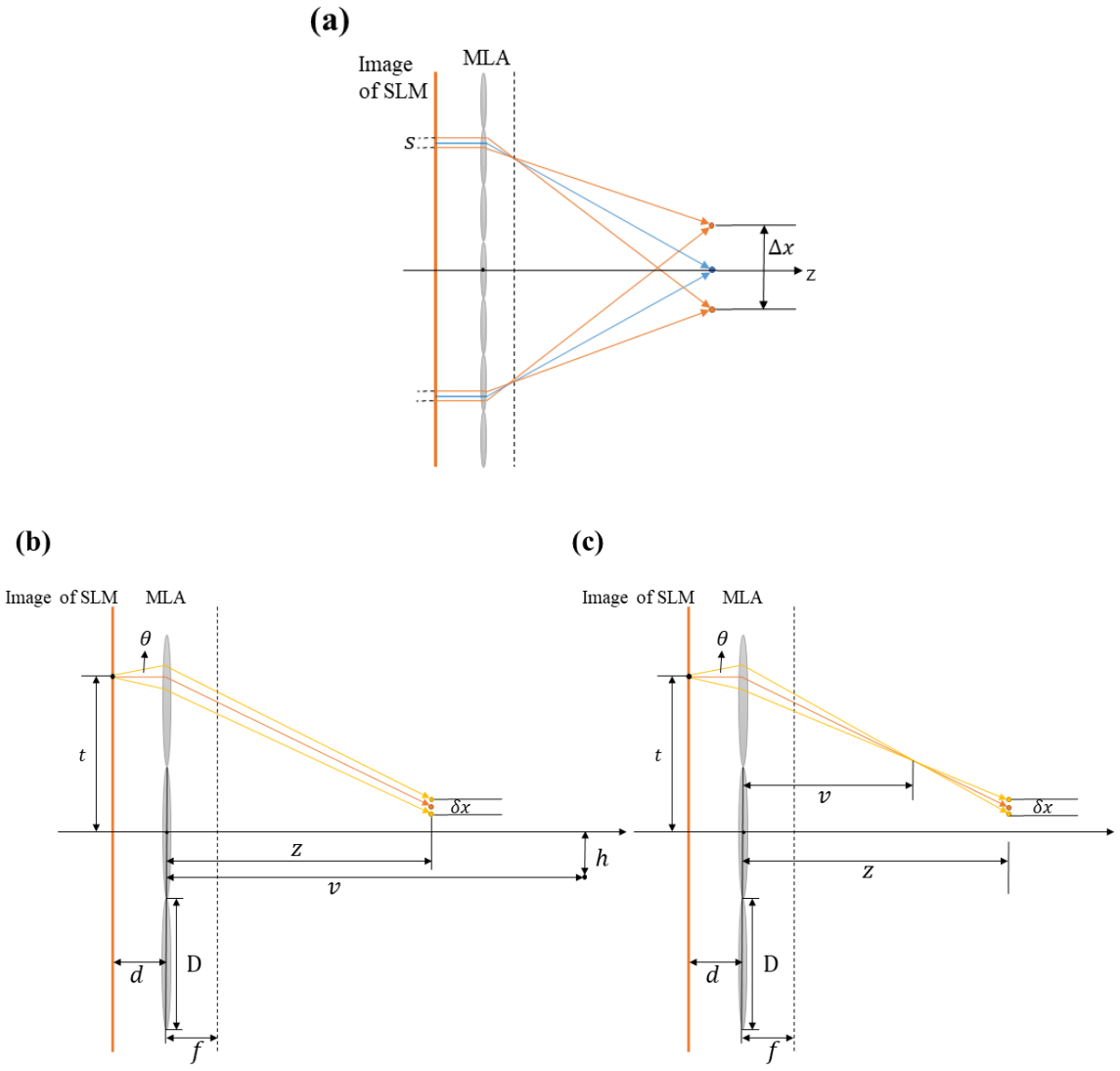
(a)
Image of SLM
MLA
s
Δx
z
(b)
Image of SLM
MLA
θ
t
δx
z
h
v
d
D
f
(c)
Image of SLM
MLA
θ
t
v
δx
z
d
D
f

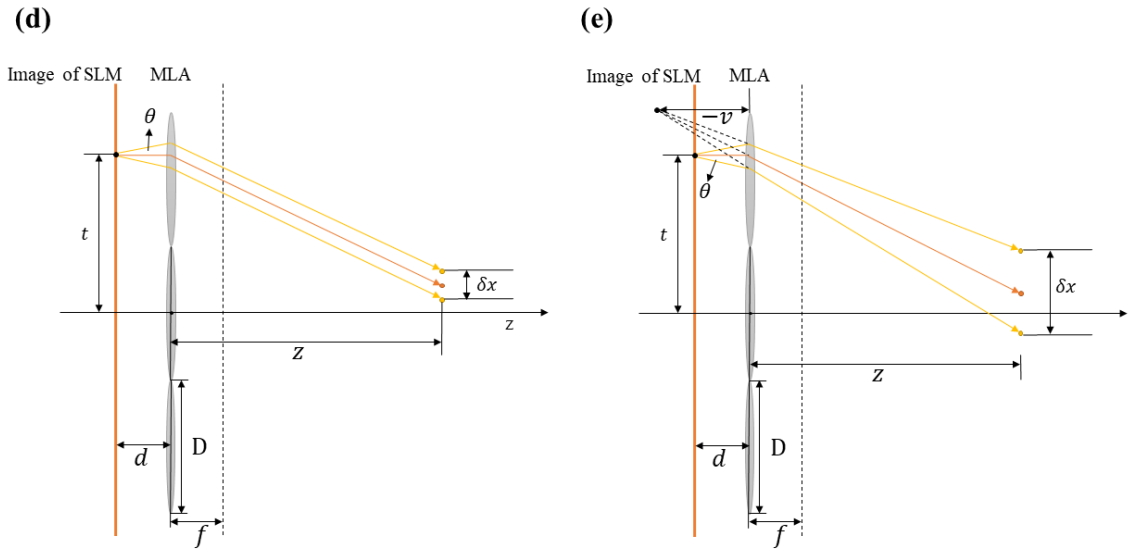

Figure 4.6 Estimation of digital lateral resolution in the light field 3D projection/photolithography system. MLA focal distance f and pitch size D. Separation distance between the relayed image of SLM and the MLA d. (a). Δx resulting from finite SLM pixel size s. Blue rays are the designed ray and the orange rays are the marginal rays from the edge of the SLM pixel; (b). δx resulting from angle of divergence θ in configuration $d > f$ when $z \leq v$, here $v = fd/(d-f)$; (c). δx resulting from angle of divergence θ in configuration $d > f$ when $z > v$; (d). δx resulting from angle of divergence θ in configuration $d = f$; (e). δx resulting from angle of divergence θ in configuration $d < f$.

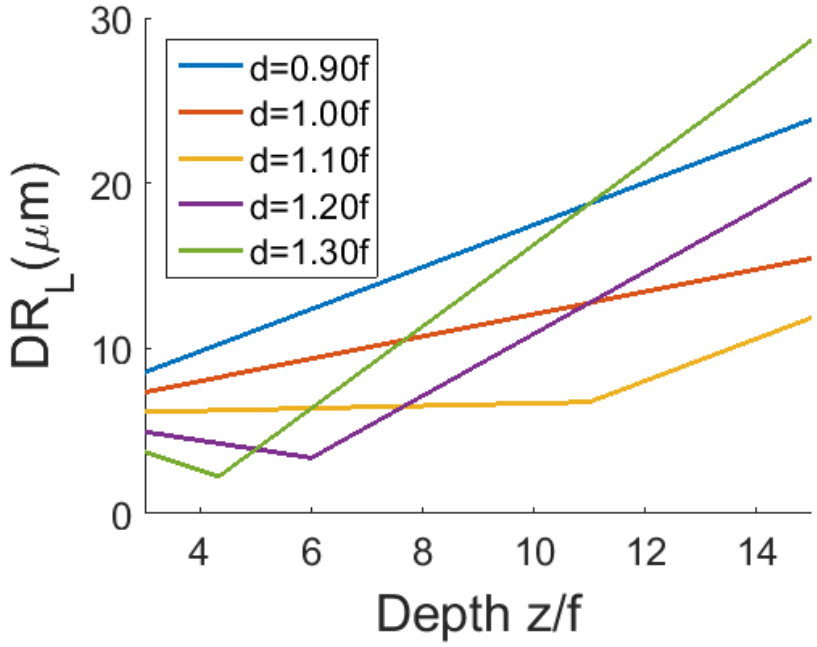

Figure 4.7 Comparison of system digital lateral resolution with different configurations of SLM and MLA combination. MLA focal distance $f = 4.8\ mm$ and pitch $D = 300\ \mu m$. Angle of divergence $\theta = 0.6°$. SLM pixel size $s = 10.8\ \mu m$.

The lateral resolution of the system is also experimentally studies. A 2x2 grid consists of single voxel wide lines are projected. The total size of the grid is $270\ \mu m \times 270\ \mu m$. The designed depth of the grid is at $z = 6$f after the MLA. The corresponding SLM pixel value map is presented in Fig. 4.8(a). The projected pattern is captured as the picture shown in Figure 4.8(b). Photolithography of SU-8 is done by expose the photoresist near the Si substrate for 8 minutes. The fabricated pattern is shown in Fig. 4.8(c), where the smallest line width is $\sim 20\ \mu m$. With the single voxel line projection, the lateral resolution of the system is verified and agree with the theoretical analysis as shown in Fig. 4.8(d).

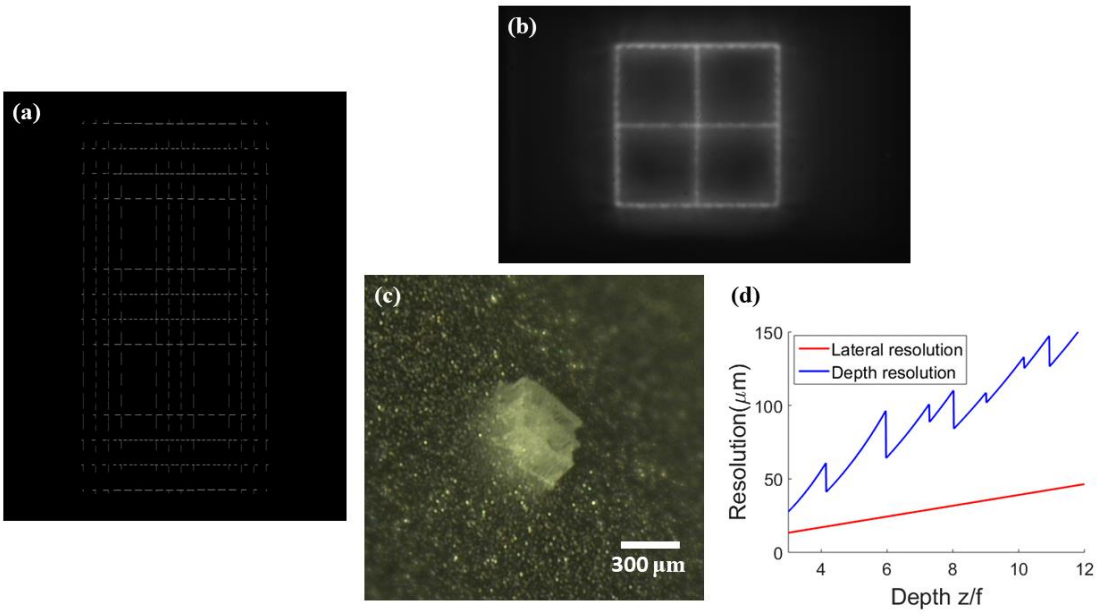

Figure 4.8 (a) Pixel value map of SLM to project the designed 2x2 grid with single voxel width; (b) Image of the the pattern projected; (c) Pictures of the fabricated pattern with 8 min exposure time. (d) Calculation of lateral and depth resolution. The system parameters are: MLA focal distance $f = 4.8\,mm$, microlens size $D = 300\,\mu m$, active region of MLA $\alpha = 0.9$, $\beta = 0.3$, angle of divergence $\theta = 0.6°$, relay image compression ratio $M = 16$, SLM pitch size $s = 10.8\,\mu m$, $d = 2.4\,mm$.

4.4.2. Depth Resolution

Optical depth resolution can be estimated similarly as optical lateral resolution,

$$OR_z = \frac{\lambda}{\sin^2 \theta_{proj}} = \lambda\left(1 + \frac{4f^2}{M^2\alpha^2 D^2}\right) \tag{4.13}$$

For wavelength $\lambda = 405\,nm$, magnification $M = 16$, MLA focal distance $f = 4.8\,mm$ and pitch $D = 300\,\mu m$, and active microlens parameter $\alpha = 1$, optical depth resolution of system $OR_z = 2.0\,\mu m$.

Regarding the digital depth resolution, the smallest voxel depth can also be attributed to the finite size of SLM pixel s and the angle of divergence θ of light beams sent to MLA.

The extent in depth near the designed projection voxel due to finite size of SLM pixel s, is Δz in Figure 4.9(a).

$$\Delta z = \frac{4iDfs(z-f)^2}{(2iDf)^2 - s^2(z-f)^2} \tag{4.14}$$

Here the microlens distance factor i has been included.

The effect of angle of divergence also depends on the configuration of the light field 3D projection system. For configuration $d > f$ when $z \leq v$ as shown in Figure 4.9(b),

$$\delta z_L = z - v\frac{iD\frac{z}{z-f} - d\tan\theta}{iD\frac{v}{z-f} - d\tan\theta} \tag{4.15}$$

$$\delta z_R = v\frac{iD\frac{z}{z-f} + d\tan\theta}{iD\frac{v}{z-f} + d\tan\theta} - z \tag{4.16}$$

For configuration $d > f$ when $z > v$ as shown in Figure 4.9(c),

$$\delta z_L = z - v\frac{iD\frac{z}{z-f} + d\tan\theta}{iD\frac{v}{z-f} + d\tan\theta} \tag{4.17}$$

$$\delta z_R = v\frac{iD\frac{z}{z-f} - d\tan\theta}{iD\frac{v}{z-f} - d\tan\theta} - z \tag{4.18}$$

For configuration $d = f$ as shown in Figure 4.9(d),

$$\delta z_L = \delta z_R = \frac{zd\ tan\,\theta}{iD\frac{z}{z-f}} \tag{4.19}$$

For configuration $d < f$ as shown in Figure 4.9(e), Equation (4.15) and (4.16) stand.

With the compression of an infinity-corrected microscope, the digital depth resolution of the light field 3D projection system is

$$DR_z = \frac{1}{M^2}[\Delta z + \delta z_L(A) + \delta z_R(B)] \tag{4.20}$$

In the expression of digital depth resolution, the microlens distance factor i has been included, which means that ligth beams converging to the voxel with different angles contribute differently to the smallest voxel depth. A larger i value may result in small voxel depth. To estimate system depth resolution, Equation (4.20) are averaged over all possible values of microlens distance factor i.

Equation (4.14) shows that using a microlens with smaller i value, can potentially reduce the resolution of projecting a voxel. Therefore, the SLM pixels corresponding to center portion of each microlens is deactivated in order to increase lithography resolution, which is controlled by parameter β in the active region.

According to Figure 4.10, Configuration $d = 1.1f$ has an overall better performance in the whole depth range $[3f, 15f]$. The system parameters used are MLA focal distance $f = 4.8\,mm$,pitch $D = 300\,\mu m$, angle of divergence $\theta = 0.6°$ and SLM pixel size $s = 10.8\,\mu m$. By comparing the system optical depth resolution and digital depth resolution, the smallest voxel depth is determined by the digital depth resolution DR_z, which is approximated $20\,\mu m$ in a large depth range.

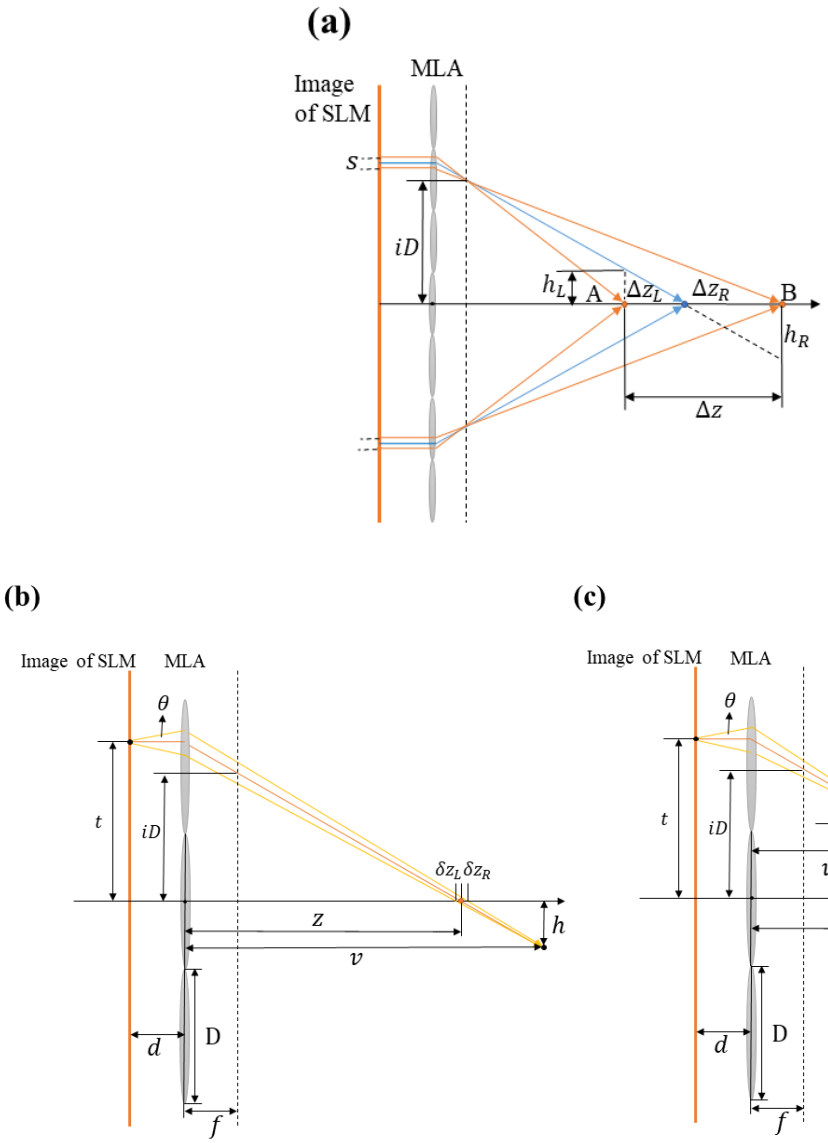
(a)
Image of SLM
MLA
s
iD
h_L
A
Δz_L
Δz_R
B
h_R
Δz
(b)
Image of SLM
MLA
θ
t
iD
δz_L δz_R
z
h
v
d
D
f
(c)
Image of SLM
MLA
θ
t
iD
v
h
δz_L δz_R
z
d
D
f

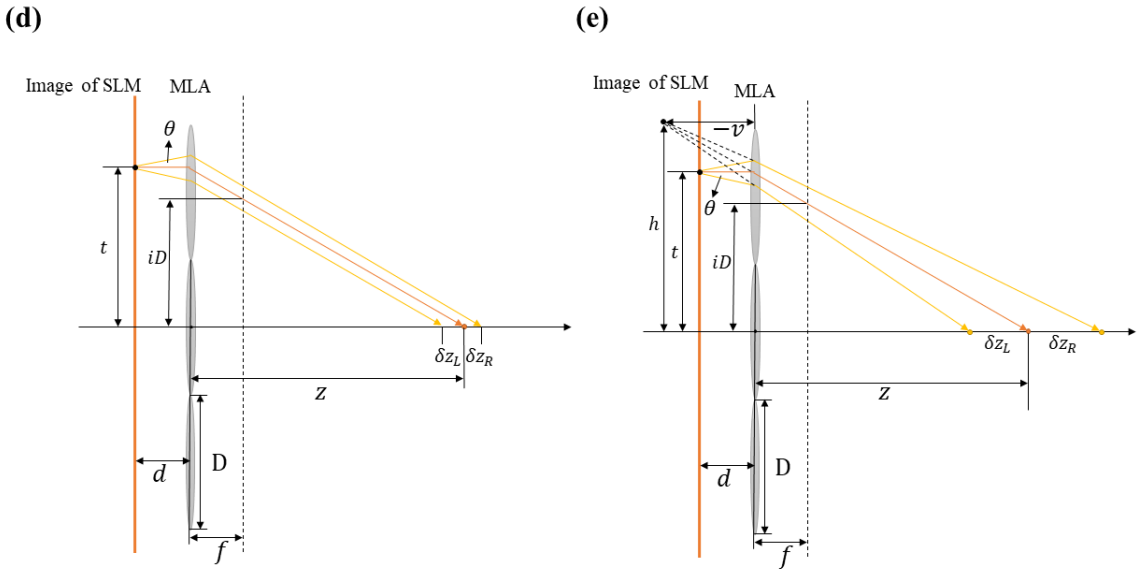

Figure 4.9 Estimation of digital depth resolution in the light field 3D projection/photolithography system. MLA focal distance f and pitch size D. Separation distance between the relayed image of SLM and the MLA d. Active microlens is iD away from the center microlens with a microlens distance factor i. (a). Δz resulting from finite SLM pixel size s. Blue rays are the designed ray and the orange rays are the marginal rays from the edge of the SLM pixel; (b). δz resulting from angle of divergence θ in configuration $d > f$ when $z \leq v$, here $v = fd/(d-f)$; (c). δz resulting from angle of divergence θ in configuration $d > f$ when $z > v$; (d). δz resulting from angle of divergence θ in configuration $d = f$; (e). δz resulting from angle of divergence θ in configuration $d < f$.

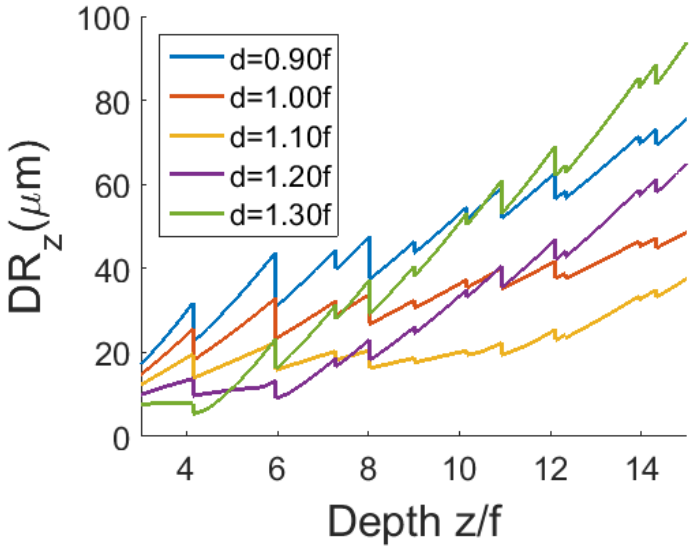

Figure 4.10 Comparison of system digital depth resolution with different configurations of SLM and MLA combination. MLA focal distance $f = 4.8\ mm$ and pitch $D = 300\ \mu m$. Angle of divergence $\theta = 0.6°$. SLM pixel size $s = 10.8\ \mu m$.

Regarding the experimental depth resolution, due to the fact of existing unwilling curing along the light path with single photon absorption, it is difficult to calibrate the voxel size in z direction (depth) experimentally. Also, the voxel size in z direction is affected by the incident ray directions when single photon absorption is used. However, we expect the depth resolution can be experimentally determined and improved by introducing femtosecond laser light source and the associated two-photon photolithography in the future work.

4.5. Result and Discussion

4.5.1. Light Field 3D Projection

In order to image the projected pattern into a CCD camera and observe directly, the infinity-corrected microscope is replaced by another telecentric lens pair with 1:1 magnification. The revised setup is illustrated in Figure 4.11. As the optical detector of the system, CCD camera is focused at different depth to verify the quality of projection.

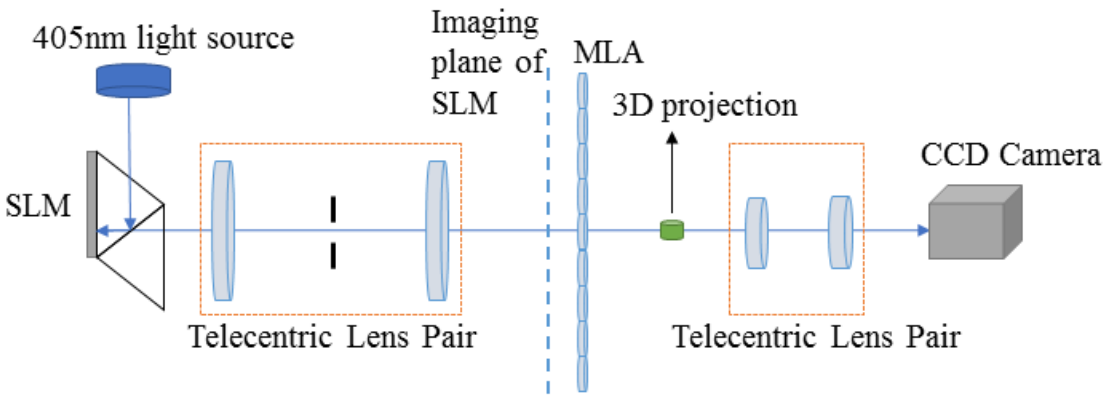

Figure 4.11 Schematic of the revised light field projection system with CCD camera imaging the 3D projected pattern directly.

Required pixel value map is generated using the algorithm discussed in Section 4.1 and loaded into SLM. The first 3D structure to be projected is shown in Figure 4.12(a). The pattern consists of two rings. The two rings are located at depths $5f$ $(24.0\ mm)$ and $6f$ $(28.8\ mm)$. When the pattern is projected, the CCD camera is focused at different focal positions in order to reveal that the projected pattern actually has structures at different depths. This is verified by Figure 4.12(b) and 4.12(c), where the inner ring and outer ring

are focused respectively. The depth difference is a direct evidence that the real 3D structure is reconstructed by the light field 3D projection.

A more complicated pattern is generated as shown in Figure 4.12(d) originating from a cone surface. Five rings are evenly distributed on the cone surface from depth $5f$ ($24.0\ mm$) to depth $8f$ ($38.4\ mm$). By translating the camera in z direction, either the inner rings or the outer rings can be focused. The quality of focusing of the outer rings in Figure 4.12(f) is not as good as the inner rings in Figure 4.12(e). This can be attributed to the lower depth resolution at deeper space and therefore larger voxel sizes are formed.

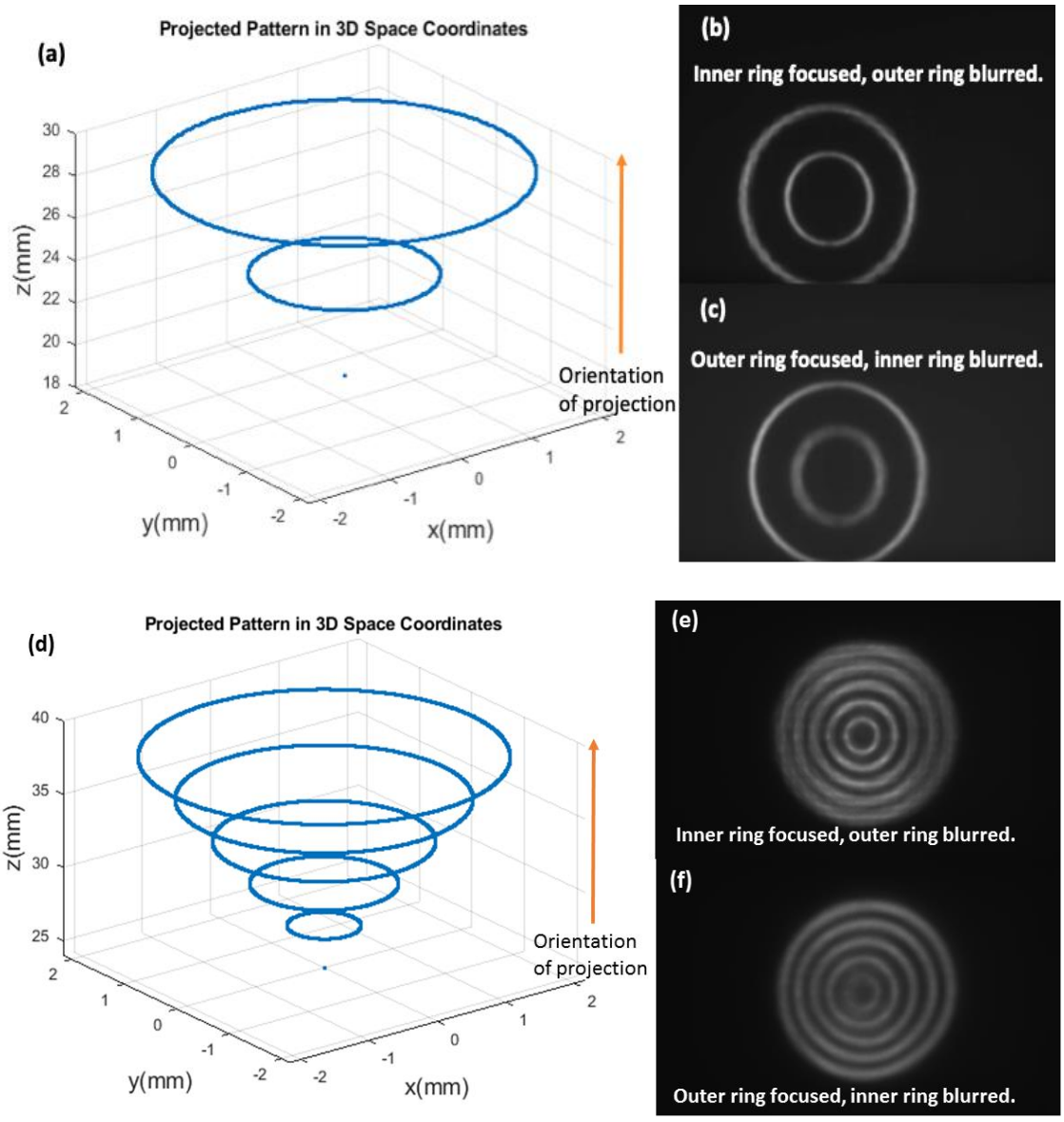

Figure 4.12 (a). Designed 3D projection from two rings at depths $5f$ $(24.0\ mm)$ and $6f$ $(28.8\ mm)$; (b). Optical image focused on the inner ring; (c). Optical image focused on the outer ring; (d). Designed 3D projection of five rings evenly distributed on the cone surface from depth $5f$ $(24.0\ mm)$ and $8f$ $(38.4\ mm)$; (e). Optical image focused on the inner rings; (f). Optical image focused on the outer rings.

4.5.2. Light Field 3D Photolithography

Permanent epoxy negative photoresist SU-8 2150 spin coated on silicon wafer has been prepared after soft baking. SU-8 sample is exposed within the light field 3D projection/photolithography system illustrated in Figure 4.2. Post exposure bake takes place right after exposure. SU-8 photoresist is cured and developed in this process to reveal the 3D structures of the intended projection.

As the first photolithography test, a conical frustum surface is designed, discretized and projected according to the procedures described above. The designed conical frustum, after the optical compression with the telecentric lens pair, has $92\,\mu m$ top diameter, $250\,\mu m$ base diameter and $112.5\,\mu m$ height. Voxels of the frustum spread from $z = 4f$ plane to $z = 10f$ plane based on the coordinate system defined in Figure 4.1. Pixel value map to project the frustum is shown in Figure 4.13(a). The MLA active region for this map is chosen as $\alpha = 0.9, \beta = 0.3$ to reduce the focused voxel size and to avoid the usage of microlens boundaries. To measure the local thickness of the SU-8 photoresist layer, full SLM pixel illumination is applied to expose the photoresist for 10 minutes. The generated overexposed pattern on the SU-8 layer is shown in Figure 4.13(b), which indicates the thickness of the SU-8 photoresist layer as $417\,\mu m$. Pixel value map is then loaded to SLM to project the designed frustum with 270 seconds exposure time. Note that the long exposure time can be attributed to low brightness of the UV LED used in the SLM illumination (approximately 150 lumens at maximum $15\,W$ power consumption). The light transport efficiency is 1.4% from the light source to the MLA. Most of light is blocked so only nearly parallel rays are used in the light field 3D projection. The low light

intensity leads to relative long exposure time when fabricating 3D structure in SU-8. Also, with 16X compression, the biggest structure can be fabricated from a single projection is $625\ \mu m \times 476\ \mu m$. Please note that even larger structures can be fabricated through translating the x-y-z positions of the sample stage.

Fabricated pattern is presented in Figure 4.13(c) and (d). Height of the fabricated structure is $318\ \mu m$, which is shorter than the thickness of photoresist layer. Tapering shape of the designed conical frustum is revealed in the SU-8 photoresist layer after development. Formation of the tapering shape indicates the benefit of 3D light field photolithography. In traditional 2D microfabrication, light beams are focused on a 2D plane parallel to the substrate. The shapes of light propagation and intensity distribution are symmetric above and below the 2D focal plane. However, in the demonstrated 3D light field projection, light rays are focused at different depths, which can result in the fabricated structure only being wider towards the bottom rather than in an hourglass shape. The deviations in the fabricated tapering angle and height compared with the designed frustum structure can be attributed to the single photon absorption of photopolymer for which curing is not limited to the designed voxel positions but also along the light path, especially around the voxels since the light intensity can be higher than the curing threshold of the SU-8 photoresist. For each voxel, there are limited number of light rays to be focused instead of a continuous focal cone of light. When limited number of light rays are applied to cure the photoresist, cured photoresist string patterns appear on the surface of the fabricated structure as in Figure 4.13(d).

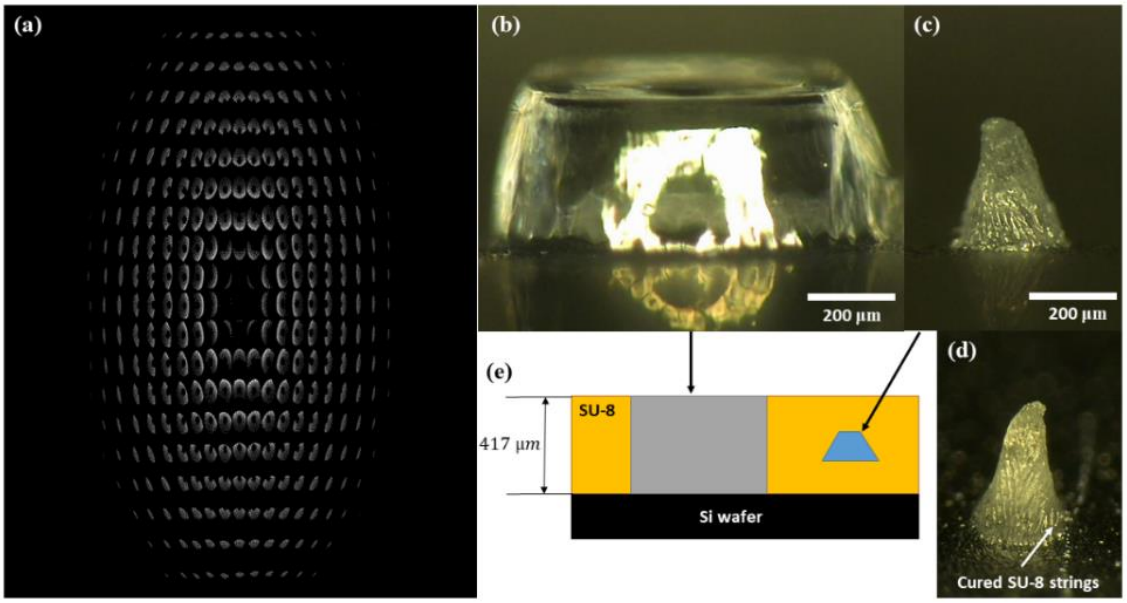

Figure 4.13 (a). Pixel value map of SLM to project the designed 3D conical frustum; (b). An overexposed pattern showing the full thickness of SU-8 photoresist layer ($417\ \mu m$); (c). Photolithography result of a conical frustum surface. Projection exposure time is 4.5 minutes. The height of fabricated pattern is $318\ \mu m$; (d). Same fabricated pattern from another angle of view; (e). Illustration of the locations of the designed pattern within the SU-8 photoresist layer.

The second photolithography test is a tilted line structure with one end attached to an overexposed wall. The designed structure is illustrated in Figure 4.14(a) with $27\ \mu m$ width, $365\ \mu m$ length (end-to-end length projected on the substrate), and $112.5\ \mu m$ height (from $z = 6f$ plane to $z = 12f$ plane) in projection. Pixel value map to project the structure is shown in Figure 4.14(b). The fabrication result is presented in Figure 4.14(c) - (e) observed from different viewing angles. The depth variation of the reconstructed tilted structure is achieved with our 3D light field photolithography technique. Length of projection of the fabricated pattern is the same as designed $365\ \mu m$. Height of the

fabricated pattern is 122 μm that is slightly higher than the designed height, which can be attributed to the unwilling curing along the light path.

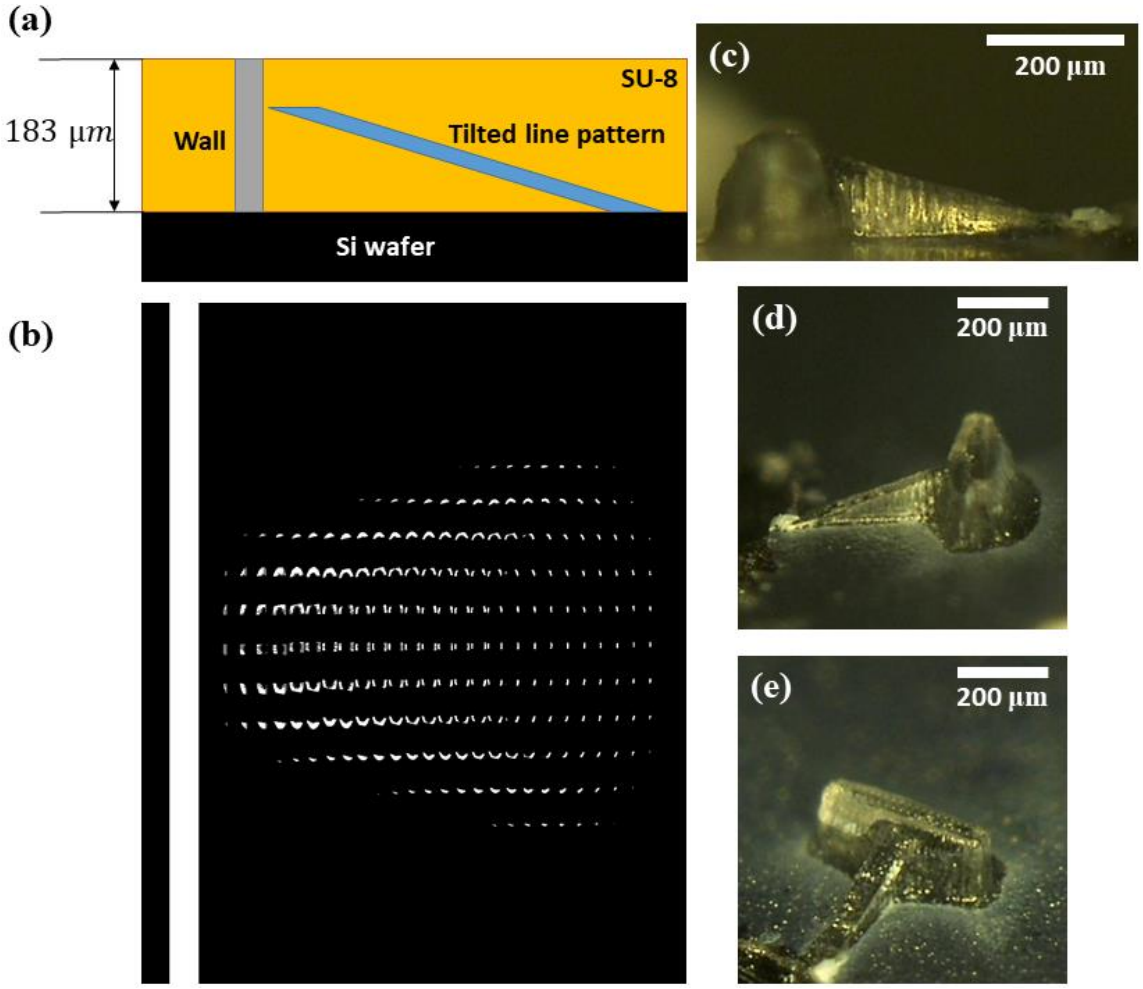

Figure 4.14 (a). Illustration of the locations of the designed tilted line structure and the wall within the SU-8 photoresist layer; (b). Pixel value map of SLM to project the designed tilted line structure; (c)-(e). Pictures of the fabricated pattern with 240 seconds exposure time from different viewing angles. Height of the wall is 183 μm. Height of fabricated pattern is 122 μm.

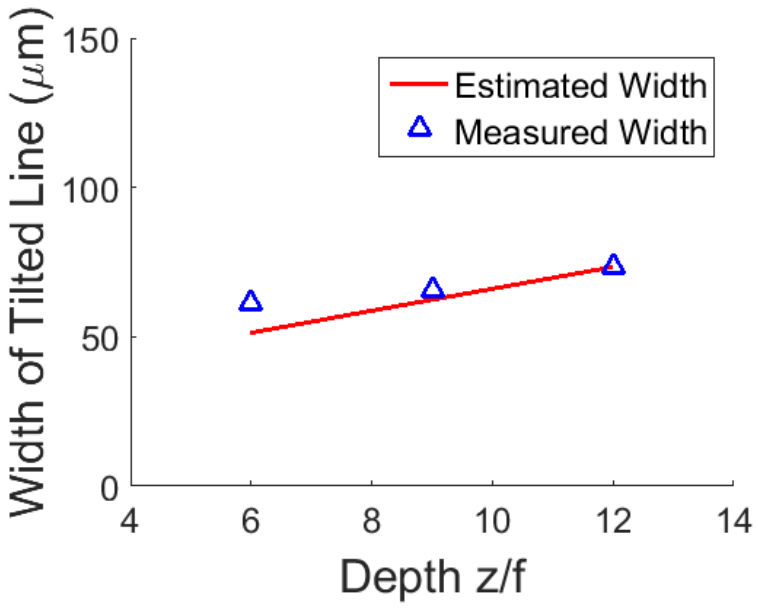

Figure 4.15 Comparison between the estimated tilted line width and the measured width of the fabricated structure at different depths. The estimated tilted line width is based on the designed tilted line pattern and the lateral resolution estimated on Section 4.4.

Width of the tilted line structure can be estimated. The designed tilted line has 9 voxels in the transverse direction with a separation distance of 3 μm with each other. Thus, the designed structure is 27 μm wide. The smallest lateral voxel size has been studied in Section 4.4. With the current SLM to MLA distance $d = 2.4\, mm$, the smallest lateral voxel size is presented in Figure 4.8(d). Hence, the estimated width of the tilted line structure is linearly distributed from 51.4 μm at top surface (depth $z = 6f$) to 73.4 μm at bottom surface (depth $z = 12f$), as plotted in Figure 4.15. Width of the fabricated pattern is measured at the three different depth $z = 6f, 9f, 12f$. By the comparison in Figure 4.15, the measured width is reasonablely close to the estimated width based on the predicted lateral resolution. The predicted model slightly underestimates width of the

fabricated tilted line structure since ideal case is considered in the model. In the photolithography experiment, factors such as imperfect SLM to MLA calibration at certain locations, or nonuniform light ray intensity converging to 3D voxels, may affect the smallest fabricated voxel size.

The fabricated patterns show the benefit of light field 3D photolithography that curing of photoresist at different depths can be controlled. Also, the light field 3D photolithography technique has the ability to improve the 3D fabrication speed significantly when an area of $> 300\,\mu m \times 300\,\mu m$ can be fabricated within a single projection since only a pixel value map is required to pattern the voxel cloud simultaneously.

4.6. Summary

A 3D photolithography method through light field 3D projection with MLA and SLM is presented. The mathematical scheme to obtain the mapping function between the voxel in a 3D space and the pixels on SLM is established. The 3D photolithography system, with the capability of focusing light rays to different depths in a 3D space, requires a calibration to determine the relative positions between the pixels of the SLM and microlenses of the MLA. The photolithography method is validated with fabrication of different 3D patterns on SU-8 negative photoresist. The 3D fabrication structures have controlled depth change which is not possible in tradition 2D single photon photolithography. The proposed method can fabricate computer designed 3D patterns in a single projection (i.e. no scanning is required). Therefore, the proposed light field 3D

photolithography has the ability to perform large area 3D fabrication with short amount of time. The fabricated shape distortion in this study is mainly due to single photon absorption and the resulting unwilling curing along the optical path of light rays. With future adoption of femtosecond light source and the associated multi-photon absorption, we expect unwilling light absorption before arriving to the voxel positions can be prevented for achieving high resolution and high precision 3D light field photolithography.

5. CONCLUSIONS AND FUTURE WORK

5.1. Conclusions

Excess heat generation during operation of microscale electronic devices has become a major concern since the heat generation can induce thermal stress and cause failure of the parts with low heat dissipation rate. Well-designed thermal management not only prolongs the working life of electronic devices but also increases their reliability Therefore, understanding temperature distribution of electronic devices is especially important in the design of optimal thermal management, which is one of the bottlenecks nowadays in developing advanced and compact micro-electronic and micro-optical devices. There exists some common thermometry and thermography techniques for measuring temperature of microscale electronic devices, such as micro-thermocouples, infrared thermography and thermoreflectance imaging. Among these thermometry and thermography techniques, thermoreflectance imaging is not only a non-contact method which does not affect the heat transfer on the target, but also an imaging method which can obtain the temperature distribution on target surface with high spatial, temporal and temperature resolution.

Thermoreflectance imaging is a non-intrusive temperature measurement method based on measuring the relative change of the reflectivity from a target surface before and after heating. A probe beam which illuminates the target is required for generating the reflection signal. Calibration of the thermoreflectance coefficient is necessary unless the material and surface condition of the target are known.

The first part of this study is to extend the traditional thermoreflectance imaging to three-dimensional so it has the ability of resolving both light direction and light intensity simultaneously. A focused light field camera is introduced as optical detector to achieve the research goal. The normal incidence assumption in traditional two-dimensional thermoreflectance no longer stands in three-dimensional cases. As a result, the expression of directional thermoreflectance coefficient of common materials has been derived with arbitrary wavelength and incident angles. With the three-dimensional thermoreflectance imaging experimental system and proper imaging data processing scheme, steady–state surface temperature measurements of microscale electronic devices including a high-power infrared laser diode and a gold wire under operation are carried out. The measured temperature distribution shows the advantage of three-dimensional thermoreflectance imaging over traditional thermoreflectance imaging, which (i) can obtain correct intensity information on curved surface with different depths; (ii) is able to resolve directional reflectivity and its contribution in thermoreflectance. The resultant thermal images indicate reasonable temperature profiles, benefits of extended depth of field and the ability to resolve reflecting directions. It is concluded that the three-dimensional thermoreflectance imaging technique can estimate temperature distributions of microscale three-dimensional tilted or curved surfaces that cannot be achieved with two-dimensional thermoreflectance imaging.

The second part of this study is to address the thermal expansion related sample movement issue in traditional thermoreflectance imaging. By adding one more wavelength of light, the two-wavelength thermoreflectance method obtains temperature

information directly from heated target under operation, therefore the movement of the target induced by thermal expansion does not affect the measurement at all unlike the traditional single-wavelength thermoreflectance. The research is achieved by a proper calibration of intensity ratio between two colors under unheated condition. The advantage of two-wavelength thermoreflectance imaging is verified by comparing the measured temperature distribution with that of traditional single wavelength thermoreflectance. Two-wavelength thermoreflectance thermal maps indicate accurate temperature values even though the effect of thermal expansion is strong in the thin film gold resistor. The results also show more true surface features and less noise on thermal maps. In addition, two-wavelength thermoreflectance imaging provides a high thermoreflectance signal than traditional single wavelength thermoreflectance when the two adopted wavelengths are appropriately selected to have opposite signs. The increased signal leads to better temperature resolution and larger signal-to-noise ratio in the measurement.

Manufacturing of modern integrated circuits and microchips involves micro-/nanolithography techniques such as electron beam lithography, focused ion beam, photolithography, etc. With the miniaturization and three-dimensional nature of microelectronic components, fabrication of microscale three-dimensional structures is required in many applications. Currently most microscale three-dimensional fabrications are done with lithography methods including single spot multiphoton photolithography, layer-by-layer stereolithography and holographic lithography. Single spot lithography can reach sub-micrometer spatial resolution, which is sufficient for most cases. However, a time consuming point-by-point scanning is required to fabricate a large-area and

complicated structure. Layer-by-layer stereolithography is faster than single spot photolithography in fabricating three-dimensional structures, but still requires a large number of perpendicular movements. Holographic lithography can pattern three-dimensional structures in single projection. However, the coherent light source in holographic lithography can cause interference patterns when complicated structures are projected, and significantly reduce the spatial resolution to tens of micrometers. In order to develop a three-dimensional lithography technique which can pattern microscale structures with fast speed (single projection) and high spatial and depth resolution, a microlens array based light field projection and photolithography system is proposed with the capability of projecting satisfactory microscale patterns and allowing sub-micrometer photolithography in the future.

The microlens array based light field projection was inspired by the light field imaging/camera, which achieves three-dimensional imaging by inserting a microlens array in a conventional camera. Light field projection works as the inverse process of the light field imaging, and reconstructs three-dimensional structures with a voxel cloud. With a spatial light modulator providing programmable light source, mathematical scheme to generate pixel value map of spatial light modulator can be determined according to ray tracing method. A theoretical analysis for the lateral and depth resolution of the projection system is also carried out. The light field projection system is validated by focusing a conventional camera at different depth of the projected patterns. The observable depth difference is a direct evidence that real three-dimensional structure is reconstructed.

Light field projection is also extended to light field photolithography. Different microscale structures with tilted/curved surfaces are fabricated in SU-8 negative photoresist via the light field photolithography system. The fabricated patterns show the benefit of light field photolithography that microfabrication at different depths can be controlled. Also, the light field photolithography system improves the 3D fabrication speed significantly when an area of $\sim 300\ \mu m \times 300\ \mu m$ can be fabricated within a single projection.

5.2. Future Work

The microlens array based light field photolithography can be extended to perform multi-photon photolithography in the future. High precision patterning is expected to be achieved when femtosecond laser light source and the associated multi-photon polymerization of photopolymers are included in the current light field projection/photolithography technique. For multi-photon photolithography methods, a spatial resolution down to below $100\ \mu m$ can be practically achieved. Multi-photon polymerization can prevent the unwilling patterning of photopolymer regions along the optical path and at the same time, push the spatial resolution into sub-micrometer range and better than diffraction limit.

To reach such research goal a femtosecond laser will replace the current light-emitting diode light source to induce multi-photon polymerization. Compared with single spot multi-photon direct laser writing, the proposed multi-photon light filed

photolithography will have similar spatial resolution/smallest voxel size, but have the ability to perform fast speed microfabrication in a large area.

REFERENCES

[1] Yao, B., P. Lai, J. Liu, and X. Liang. “The Effect of Thermal Stress on High Density Packaging Integrated Circuits.” 2011 International Symposium on Advanced Packaging Materials (APM), 2011. doi:10.1109/isapm.2011.6105693.

[2] Suhir, E. “Thermal Stress Failures in Electronics and Photonics: Physics, Modeling, Prevention.” Journal of Thermal Stresses 36, no. 6 (2013): 537–63. Doi:10.1080/01495739.2013.784119.

[3] Anandan, S. S. and V. Ramalingam. "Thermal Management of Electronics: A Review of Literature." Thermal Science 12, no. 2 (2008): 5-26. doi:10.2298/tsci0802005a.

[4] Mcglen, R. J., R. Jachuck, and S. Lin. "Integrated Thermal Management Techniques for High Power Electronic Devices." Applied Thermal Engineering 24, no. 8-9 (2004): 1143-156. doi:10.1016/j.applthermaleng.2003.12.029.

[5] Amon, C. H., J. Murthy, S. C. Yao, S. Narumanchi, C-F. Wu, and C-C. Hsieh. "MEMS-enabled Thermal Management of High-heat-flux Devices EDIFICE: Embedded Droplet Impingement for Integrated Cooling of Electronics." Experimental Thermal and Fluid Science 25, no. 5 (2001): 231-42. doi:10.1016/s0894-1777(01)00071-1.

[6] Kölzer, J., E. Oesterschulze, and G. Deboy. "Thermal Imaging and Measurement Techniques for Electronic Materials and Devices." Microelectronic Engineering 31, no. 1-4 (1996): 251-70. doi:10.1016/0167-9317(95)00348-7.

[7] Blackburn, D. L. “Temperature Measurements of Semiconductor Devices - a Review.” Twentieth Annual IEEE Semiconductor Thermal Measurement and Management Symposium (IEEE Cat. No.04CH37545), n.d. doi:10.1109/stherm.2004.1291304.

[8] Kim, M. M., A. Giry, M. Mastiani, G. O. Rodrigues, A. Reis, and P. Mandin. “Microscale Thermometry: A Review.” Microelectronic Engineering 148 (2015): 129–42. doi:10.1016/j.mee.2015.11.002.

[9] Trigg, A. "Applications of Infrared Microscopy to IC and MEMS Packaging." IEEE Transactions on Electronics Packaging Manufacturing 26, no. 3 (2003): 232-38. doi:10.1109/tepm.2003.820807.

[10] Kateb, B., V. Yamamoto, C. Yu, W. Grundfest, and J. P. Gruen. “Infrared Thermal Imaging: A Review of the Literature and Case Report.” NeuroImage 47 (2009). doi:10.1016/j.neuroimage.2009.03.043.

[11] Csendes, A., V. Székely, and M. Rencz. "Thermal Mapping with Liquid Crystal Method." Microelectronic Engineering 31, no. 1-4 (1996): 281-90. doi:10.1016/0167-9317(95)00350-9.

[12] Popov, V. M., A. S. Klimenko, A. P. Pokanevich, I. I. Gavrilyuk, and N. V. Moshel.’ “Liquid-Crystal Thermography of Hot Spots on Electronic Components.” Russian Microelectronics 36, no. 6 (2007): 392–401. doi:10.1134/s1063739707060066.

[13] Pylkki, R. J., P. J. Moyer, and P. E. West. “Scanning Near-Field Optical Microscopy and Scanning Thermal Microscopy.” Japanese Journal of Applied Physics 33, no. Part 1, No. 6B (1994): 3785–90. doi:10.1143/jjap.33.3785.

[14] Gomès, S., A. Assy, and P-O. Chapuis. "Scanning Thermal Microscopy: A Review." Physica Status Solidi (a) 212, no. 3 (2015): 477-94. doi:10.1002/pssa.201400360.

[15] Kuball, M., J. M. Hayes, M. J. Uren, T. Martin, J. C. H. Birbeck, R. S. Balmer, and B. T. Hughes. "Measurement of Temperature in Active High-power AlGaN/GaN HFETs Using Raman Spectroscopy." IEEE Electron Device Letters 23, no. 1 (2002): 7-9. doi:10.1109/55.974795.

[16] Chatterjee, B., A. Jayawardena, E. Heller, D. W. Snyder, S. Dhar, and S. Choi. "Thermal Characterization of Gallium Oxide Schottky Barrier Diodes." Review of Scientific Instruments 89, no. 11 (2018): 114903. doi:10.1063/1.5053621.

[17] Grauby, S., S. Dilhaire, S. Jorez, and W. Claeys. “Temperature Variation Mapping of a Microelectromechanical System by Thermoreflectance Imaging.” IEEE Electron Device Letters 26, no. 2 (2005): 78–80. doi:10.1109/led.2004.841468.

[18] Farzaneh, M., K. Maize, D. Lüerßen, J. A. Summers, P. M. Mayer, P. E. Raad, K. P. Pipe, A. Shakouri, R. J. Ram, and Janice A. Hudgings. "CCD-based Thermoreflectance Microscopy: Principles and Applications." Journal of Physics D: Applied Physics 42, no. 14 (2009): 143001. doi:10.1088/0022-3727/42/14/143001.

[19] Rohsenow, W. M., J. P. Harnett, and Y. I. Cho. Handbook of Heat Transfer. Boston, MA: McGraw-Hill, 1998.

[20] Chu, D., D. T. Bilir, R. F. W. Pease, and K. E. Goodson. “Submicron Thermocouple Measurements of Electron-Beam Resist Heating.” Journal of Vacuum Science & Technology B: Microelectronics and Nanometer Structures 20, no. 6 (2002): 3044. doi:10.1116/1.1523023.

[21] Attia, M. H., and L. Kops. “Distortion in Thermal Field Around Inserted Thermocouples in Experimental Interfacial Studies—Part II: Effect of the Heat Flow Through the Thermocouple.” Journal of Engineering for Industry 110, no. 1 (1988): 7–14. doi:10.1115/1.3187847.

[22] Majumdar, A., J. Lai, M. Chandrachood, O. Nakabeppu, Y. Wu, and Z. Shi. “Thermal Imaging by Atomic Force Microscopy Using Thermocouple Cantilever Probes.” Review of Scientific Instruments 66, no. 6 (1995): 3584–92. doi:10.1063/1.1145474.

[23] Christofferson, J., K. Maize, Y. Ezzahri, J. Shabani, X. Wang, and A. Shakouri. "Microscale and Nanoscale Thermal Characterization Techniques." Journal of Electronic Packaging 130, no. 4 (2008): 041101. doi:10.1115/1.2993145.

[24] Liu, W. and B. Yang. "Thermography techniques for integrated circuits and semiconductor devices." Sensor Review 27, no. 4 (2007): 298-309. doi:10.1108/02602280710821434.

[25] Piwonski, T., Pierścińska, D. Wawer, M. Szymański, T. Ochalski, and M. Bugajski. "Thermoreflectance study of temperature distribution on the semiconductor laser mirrors." Optica Applicata 35, no. 3(2005).

[26] Thorne, S. A., S. B. Ippolito, M. S. Ünlü, and B. B. Goldberg. “High-Resolution Thermoreflectance Microscopy.” MRS Proceedings 738 (2002). doi:10.1557/proc-738-g12.9.

[27] Scouler, W. J. “Temperature-Modulated Reflectance of Gold from 2 to 10 EV.” Physical Review Letters 18, no. 12 (1967): 445–48. doi:10.1103/physrevlett.18.445.

[28] Tessier, G., S. Holé, and D. Fournier. "Quantitative Thermal Imaging by Synchronous Thermoreflectance with Optimized Illumination Wavelengths." Applied Physics Letters 78, no. 16 (2001): 2267-269. doi:10.1063/1.1363696.

[29] Rosei, R., and D. W. Lynch. “Thermomodulation Spectra of Al, Au, and Cu.” Physical Review B 5, no. 10 (1972): 3883–94. doi:10.1103/physrevb.5.3883.

[30] Fan, H. Y. “Temperature Dependence of the Energy Gap in Monatomic Semiconductors.” Physical Review 78, no. 6 (1950): 808–9. doi:10.1103/physrev.78.808.2.

[31] Batz, B. “Thermoreflectance in Germanium.” Solid State Communications 5, no. 12 (1967): 985–89. doi:10.1016/0038-1098(67)90483-8.

[32] Matatagui, E., A. G. Thompson, and Manuel Cardona. “Thermoreflectance in Semiconductors.” Physical Review 176, no. 3 (1968): 950–60. doi:10.1103/physrev.176.950.

[33] Weakliem, H. A., and D. Redfield. “Temperature Dependence of the Optical Properties of Silicon.” Journal of Applied Physics 50, no. 3 (1979): 1491–93. doi:10.1063/1.326135.

[34] Anderegg, M., B. Feuerbacher, and B. Fitton. “Thermoreflectance of Graphite.” Physical Review Letters 26, no. 13 (1971): 760–62. doi:10.1103/physrevlett.26.760.

[35] Guidotti, D., and H. M. Van Driel. "Spatially Resolved Defect Mapping in Semiconductors Using Laser-modulated Thermoreflectance." Applied Physics Letters 47, no. 12 (1985): 1336-338. doi:10.1063/1.96272.

[36] Ju, Y. S., and K. E. Goodson. “Short-Time-Scale Thermal Mapping of Microdevices Using a Scanning Thermoreflectance Technique.” Journal of Heat Transfer 120, no. 2 (1998): 306–13. doi:10.1115/1.2824246.

[37] Christofferson, J., and A. Shakouri. “Thermoreflectance Based Thermal Microscope.” Review of Scientific Instruments 76, no. 2 (2005): 024903. doi:10.1063/1.1850632.

[38] Komarov, P. A., Mihai G. Burzo and P. E. Raad. “CCD thermoreflectance thermography system: methodology and experimental validation.” (2006).

[39] Soni, A., and S-B. Wen. "Non-intrusive Temperature Measurement of NSOM Probes with Thermoreflectance Imaging." Journal of Physics D: Applied Physics 45, no. 18 (2012): 185101. doi:10.1088/0022-3727/45/18/185101.

[40] Mayer, P. M., D. Lüerßen, R. J. Ram, and J. A. Hudgings. "Theoretical and Experimental Investigation of the Thermal Resolution and Dynamic Range of

CCD-based Thermoreflectance Imaging." Journal of the Optical Society of America A 24, no. 4 (2007): 1156. doi:10.1364/josaa.24.001156.

[41] Elahi, Mirza M. "Thermoreflectance Technique for Thermal Properties Measurement of Micro/Nanoscale Cantilever Beams." (2017).

[42] Maize, K., Christofferson J, and A. Shakouri. “Transient Thermal Imaging Using Thermoreflectance.” 2008 24th Annual IEEE Semionductor Thermal Measurement and Management Symposium, 2008. doi:10.1109/stherm.2008.4509366.

[43] Vermeersch, B., J. Christofferson, K. Maize, A. Shakouri, and G. De Mey. “Time and Frequency Domain CCD-Based Thermoreflectance Techniques for High-Resolution Transient Thermal Imaging.” 2010 26th Annual IEEE Semiconductor Thermal Measurement and Management Symposium (SEMI-THERM), 2010. Doi:10.1109/stherm.2010.5444287.

[44] Jiang, Puqing, Xin Qian, and Ronggui Yang. “Tutorial: Time-Domain Thermoreflectance (TDTR) for Thermal Property Characterization of Bulk and Thin Film Materials.” Journal of Applied Physics 124, no. 16 (2018): 161103. doi:10.1063/1.5046944.

[45] Sundaram, Vijay M., Alok Soni, and Sy-Bor Wen. "Transient Temperature Response of near Field Scanning Optical Microscope Probes under Pulsed Illumination." Journal of Applied Physics 115, no. 23 (2014): 234903. doi:10.1063/1.4883539.

[46] Adelson, E. H., and J. R. Bergen. "The plenoptic function and the elements of early vision." Cambridge, MA: Vision and Modeling Group, Media Laboratory, Massachusetts Institute of Technology, 1991.

[47] Adelson, E.H., and J.Y.A. Wang. “Single Lens Stereo with a Plenoptic Camera.” IEEE Transactions on Pattern Analysis and Machine Intelligence 14, no. 2 (1992): 99–106. doi:10.1109/34.121783.

[48] Ng, R., M. Levoy, M. Bredif, G. Duval, M. Horowitz, and P. Hanrahan. "Light Field Photography with a Hand-Held Plenoptic Camera." Stanford University Computer Science Tech Report CSTR 2005-02.

[49] Georgiev, T. G., and A. Lumsdaine. "Superresolution with Plenoptic 2.0 Cameras." Frontiers in Optics 2009/Laser Science XXV/Fall 2009 OSA Optics & Photonics Technical Digest, 2009. doi:10.1364/srs.2009.stua6.

[50] Georgiev, T. G., and A. Lumsdaine. "Depth of Field in Plenoptic Cameras." Eurographics 2009-Annex (Apr. 2009), pp. 5-8.

[51] Perwass, C., and L. Wietzke. "Single lens 3D-camera with extended depth-of-field." Human Vision and Electronic Imaging XVII, 2012. doi:10.1117/12.909882.

[52] Groves, T. R., and R. A. Kendall. “Distributed, Multiple Variable Shaped Electron Beam Column for High Throughput Maskless Lithography,” Journal of Vacuum Science & Technology B: Microelectronics and Nanometer Structures 16, no. 6 (1998): p. 3168. doi:10.1116/1.590458.

[53] Li, M., L. Chen, and S. Y. Chou. “Direct Three-Dimensional Patterning Using Nanoimprint Lithography,” Applied Physics Letters 78, no. 21 (2001): pp. 3322-3324. doi:10.1063/1.1375006.

[54] Judy, J. W. “Microelectromechanical Systems (MEMS): Fabrication, Design and Applications,” Smart Materials and Structures 10, no. 6 (2001): pp. 1115-1134. doi:10.1088/0964-1726/10/6/301.

[55] Weibel, D. B., W. R. Diluzio, and G. M. Whitesides. “Microfabrication Meets Microbiology,” Nature Reviews Microbiology 5, no. 3 (2007): pp. 209-218. doi:10.1038/nrmicro1616.

[56] Pease, R. F., and S. Y. Chou. “Lithography and Other Patterning Techniques for Future Electronics.” Proceedings of the IEEE 96, no. 2 (2008): 248–70. doi:10.1109/jproc.2007.911853.

[57] Zhang, Y., J. Luo, Z. Xiong, H. Liu, L. Wang, Y. Gu, Z. Lu, J. Li, and J. Huang. “User-Defined Microstructures Array Fabricated by DMD Based Multistep Lithography with Dose Modulation.” Optics Express 27, no. 22 (2019): 31956. doi:10.1364/oe.27.031956.

[58] Vieu, C., F. Carcenac, A. Pépin, Y. Chen, M. Mejias, A. Lebib, L. Manin-Ferlazzo, L. Couraud, and H. Launois. "Electron beam lithography: resolution limits and applications." Applied Surface Science,Volume 164, Issues 1–4, 2000, doi:10.1016/S0169-4332(00)00352-4.

[59] Altissimo, Matteo. "E-beam Lithography for Micro-/nanofabrication." Biomicrofluidics 4, no. 2 (2010): 026503. doi:10.1063/1.3437589.

[60] Chen, Y. “Nanofabrication by Electron Beam Lithography and Its Applications: A Review.” Microelectronic Engineering 135 (2015): 57–72. doi:10.1016/j.mee.2015.02.042.

[61] Melngailis, J. "Focused Ion Beam Microfabrication." Electron-Beam, X-Ray, and Ion Beam Technology: Submicrometer Lithographies VII, 1988. doi:10.1117/12.945634.

[62] Watt, F., A. A. Bettiol, J. A. Van Kan, E. J. Teo, and M. B. H. Breese. "Ion beam lithography and nanofabrication: a review." International Journal of NanoscienceVol. 04, No. 03, pp. 269-286 (2005). doi:10.1142/S0219581X05003139.

[63] Volkert, C. A. and A. M. Minor. “Focused Ion Beam Microscopy and Micromachining.” MRS Bulletin 32, no. 5 (2007): 389–99. doi:10.1557/mrs2007.62.

[64] Levenson, M. D., N. S. Viswanathan, and R. A. Simpson. “Improving Resolution in Photolithography with a Phase-Shifting Mask.” IEEE Transactions on Electron Devices 29, no. 12 (1982): 1828–36. doi:10.1109/t-ed.1982.21037.

[65] Adrega, T. and S. P. Lacour. “Stretchable Gold Conductors Embedded in PDMS and Patterned by Photolithography: Fabrication and Electromechanical Characterization.” Journal of Micromechanics and Microengineering 20, no. 5 (2010): 055025. doi:10.1088/0960-1317/20/5/055025.

[66] Niesler, F. and M. Hermatschweiler. “Additive Manufacturing of Micro-sized Parts.” LTJ, 11: 16-18. (2014). doi:10.1002/latj.201400048

[67] Otter, W. J. and S. Lucyszyn. “3-D Printing of Microwave Components for 21st Century Applications,” 2016 IEEE MTT-S International Microwave Workshop Series on Advanced Materials and Processes for RF and THz Applications (IMWS-AMP), 2016. doi:10.1109/imws-amp.2016.7588327.

[68] Sundararaghavan, V. and N. Zabaras. “Classification and Reconstruction of Three-Dimensional Microstructures Using Support Vector Machines,” Computational Materials Science 32, no. 2 (2005): pp. 223-239. doi:10.1016/j.commatsci.2004.07.004.

[69] Postiglione, G., G. Natale, G. Griffini, M. Levi, and S. Turri. “Conductive 3D Microstructures by Direct 3D Printing of Polymer/Carbon Nanotube Nanocomposites via Liquid Deposition Modeling,” Composites Part A: Applied Science and Manufacturing 76 (2015): pp. 110-114. doi:10.1016/j.compositesa.2015.05.014.

[70] Liu, B., X. Gong, and W.J. Chappell. "Applications of Layer-by-Layer Polymer Stereolithography for Three-Dimensional High-Frequency Components." IEEE Transactions on Microwave Theory and Techniques 52, no. 11 (2004): 2567-575. doi:10.1109/tmtt.2004.837165.

[71] Huang, Y., X. Gong, S. Hajela, and W. J. Chappell. “Layer-by-Layer Stereolithography of Three-Dimensional Antennas.” 2005 IEEE Antennas and Propagation Society International Symposium, n.d. doi:10.1109/aps.2005.1551302.

[72] Delhote, N., D. Baillargeat, S. Verdeyme, C. Delage, and C. Chaput. “Ceramic Layer-By-Layer Stereolithography for the Manufacturing of 3-D Millimeter-Wave Filters.” IEEE Transactions on Microwave Theory and Techniques 55, no. 3 (2007): 548–54. doi:10.1109/tmtt.2007.891690.

[73] Vaezi, M., H. Seitz, and S. Yang. “A Review on 3D Micro-Additive Manufacturing Technologies.” The International Journal of Advanced Manufacturing Technology 67, no. 5-8 (2012): 1721–54. doi:10.1007/s00170-012-4605-2.

[74] Maas, J., B. Liu, S. Hajela, Y. Huang, X. Gong, and W. J. Chappell. “Laser-Based Layer-by-Layer Polymer Stereolithography for High-Frequency Applications,” Proceedings of the IEEE 105, no. 4 (2017): pp. 645-654. doi:10.1109/jproc.2016.2629179.

[75] Kunwar, P., Z. Xiong, Y. Zhu, H. Li, A. Filip, and P. Soman. “Hybrid Laser Printing of 3D, Multiscale, Multimaterial Hydrogel Structures.” Advanced Optical Materials 7, no. 21 (2019): 1900656. doi:10.1002/adom.201900656.

[76] Lan, P-T., S-Y. Chou, L-L. Chen, and D. Gemmill. “Determining Fabrication Orientations for Rapid Prototyping with Stereolithography Apparatus.” Computer-Aided Design 29, no. 1 (1997): 53–62. doi:10.1016/s0010-4485(96)00049-8.

[77] Campbell, M., D. N. Sharp, M. T. Harrison, R. G. Denning, and A. J. Turberfield. “Fabrication of Photonic Crystals for the Visible Spectrum by Holographic Lithography.” Nature 404, no. 6773 (2000): 53–56. doi:10.1038/35003523.

[78] Wang, X., J. F. Xu, H. M. Su, Z. H. Zeng, Y. L. Chen, H. Z. Wang, Y. K. Pang, and W. Y. Tam. “Three-Dimensional Photonic Crystals Fabricated by Visible Light Holographic Lithography.” Applied Physics Letters 82, no. 14 (July 2003): 2212–14. doi:10.1063/1.1565682.

[79] Liu, Y., S. Liu, and X. Zhang. "Fabrication of Three-dimensional Photonic Crystals with Two-beam Holographic Lithography." Applied Optics 45, no. 3 (2006): 480. doi:10.1364/ao.45.000480.

[80] Kondo, T., S. Juodkazis, V. Mizeikis, S. Matsuo, and H. Misawa. “Fabrication of Three-Dimensional Periodic Microstructures in Photoresist SU-8 by Phase-Controlled Holographic Lithography.” New Journal of Physics 8, no. 10 (2006): 250–50. doi:10.1088/1367-2630/8/10/250.

[81] Stay, J. L., G. M. Burrow, and T. K. Gaylord. “Three-Beam Interference Lithography Methodology.” Review of Scientific Instruments 82, no. 2 (2011): 023115. doi:10.1063/1.3535557.

[82] Cheng, Y-C., A. Isoyan, J. Wallace, M. Khan, and F. Cerrina. “Extreme Ultraviolet Holographic Lithography: Initial Results.” Applied Physics Letters 90, no. 2 (August 2007): 023116. doi:10.1063/1.2430774.

[83] Hsu, W-F., and C-F. Yeh. “Speckle Suppression in Holographic Projection Displays Using Temporal Integration of Speckle Images from Diffractive Optical Elements.” Applied Optics 50, no. 34 (2011). doi:10.1364/ao.50.000h50.

[84] Wu, E-S., J. H. Strickler, W. R. Harrell, and W. W. Webb. “Two-Photon Lithography for Microelectronic Application.” Optical/Laser Microlithography V, 1992. doi:10.1117/12.130367.

[85] Haske, W., V. W. Chen, J. M. Hales, W. Dong, S. Barlow, S. R. Marder, and J. W. Perry. "65 nm Feature Sizes Using Visible Wavelength 3-D Multiphoton Lithography." Optics Express 15, no. 6 (2007): 3426. doi:10.1364/oe.15.003426.

[86] Lee, S-H., J. J. Moon, and J. L. West. “Three-Dimensional Micropatterning of Bioactive Hydrogels via Two-Photon Laser Scanning Photolithography for Guided 3D Cell Migration.” Biomaterials 29, no. 20 (2008): 2962–68. doi:10.1016/j.biomaterials.2008.04.004.

[87] Gan, Z., Y. Cao, R. A. Evans, and M. Gu. “Three-Dimensional Deep Sub-Diffraction Optical Beam Lithography with 9 Nm Feature Size.” Nature Communications 4, no. 1 (2013). doi:10.1038/ncomms3061.

[88] Selimis, A., V. Mironov, and M. Farsari. “Direct Laser Writing: Principles and Materials for Scaffold 3D Printing.” Microelectronic Engineering 132 (2015): 83–89. doi:10.1016/j.mee.2014.10.001.

[89] Maruo, S., O. Nakamura, and S. Kawata. “Three-Dimensional Microfabrication with Two-Photon-Absorbed Photopolymerization.” Optics Letters 22, no. 2 (1997): 132. doi:10.1364/ol.22.000132.

[90] Fischer, J. and M. Wegener, “Three-Dimensional Optical Laser Lithography beyond the Diffraction Limit,” Laser & Photonics Reviews 7, no. 1 (2012): pp. 22-44. doi:10.1002/lpor.201100046.

[91] Zhou, X., Y. Hou, and J. Lin. “A Review on the Processing Accuracy of Two-Photon Polymerization.” AIP Advances 5, no. 3 (2015): 030701. doi:10.1063/1.4916886.

[92] Jonušauskas, L., D.Gailevičius, S. Rekštytė, S. Juodkazis, and M. Malinauskas, "Synchronization of linear stages and galvo-scanners for efficient direct laser fabrication of polymeric 3D meso-scale structures," Proc. SPIE 10523, Laser 3D Manufacturing V, 105230X (26 February 2018). doi:10.1117/12.2287669

[93] Kato, J-I., N. Takeyasu, Y. Adachi, H-B. Sun, and S. Kawata. “Multiple-Spot Parallel Processing for Laser Micronanofabrication.” Applied Physics Letters 86, no. 4 (2005): 044102. doi:10.1063/1.1855404.

[94] Howell, J. R., M. P. Mengüç, and R. Siegel. "Thermal radiation heat transfer." Boca Raton: CRC Press, 2011.

[95] Wilson, R. B., B. A. Apgar, L. W. Martin, and D. G. Cahill. "Thermoreflectance of metal transducers for optical pump-probe studies of thermal properties." Optics Express 20, no. 27 (2012): 28829. doi:10.1364/oe.20.028829.

[96] Rakić, A. D., A. B. Djurišić, J. M. Elazar, and M. L. Majewski. "Optical properties of metallic films for vertical-cavity optoelectronic devices." Applied Optics 37, no. 22 (1998): 5271. doi:10.1364/ao.37.005271.

[97] Shakouri, A., A. Ziabari, D. Kendig, J-H. Bahk, Y. Xuan, P. D. Ye, K. Yazawa, and A. Shakouri. "Stable Thermoreflectance Thermal Imaging Microscopy with Piezoelectric Position Control." 2016 32nd Thermal Measurement, Modeling &

Management Symposium (SEMI-THERM), 2016. doi:10.1109/semi-therm.2016.7458456.

[98] Wen, S-B., A. Bhaskar, and H. Zhang. "Scanning Digital Lithography Providing High Speed Large Area Patterning with Diffraction Limited Sub-micron Resolution." Journal of Micromechanics and Microengineering 28, no. 7 (2018): 075011. doi:10.1088/1361-6439/aabb1f.

[99] Burzo, M. G., P. L. Komarov, and P. E. Raad. "Optimized Thermo-reflectance System for Measuring the Thermal Properties of Thin-films and Their Interfaces." Twenty-Second Annual IEEE Semiconductor Thermal Measurement And Management Symposium. doi:10.1109/stherm.2006.1625211.

[100] Beran, A. "The Reflectance Behaviour of Gold at Temperatures up to 500C." TMPM Tschermaks Mineralogische Und Petrographische Mitteilungen 34, no. 3-4 (1985): 211-15. doi:10.1007/bf01082962.

[101] Soni, A., V. M. Sundaram, and S-B. Wen. "A Methodology for Nanosecond (or Better) Time Resolved Thermoreflectance Imaging with Coherence Control of Laser Pulses." Applied Physics Letters 102, no. 20 (2013): 203112. doi:10.1063/1.4807598.